creative commons
COMMONS DEED

저작자표시-비영리-변경금지 2.0 대한민국

이용자는 아래의 조건을 따르는 경우에 한하여 자유롭게

- 이 저작물을 복제, 배포, 전송, 전시, 공연 및 방송할 수 있습니다.

다음과 같은 조건을 따라야 합니다:

저작자표시. 귀하는 원저작자를 표시하여야 합니다.

비영리. 귀하는 이 저작물을 영리 목적으로 이용할 수 없습니다.

변경금지. 귀하는 이 저작물을 개작, 변형 또는 가공할 수 없습니다.

- 귀하는, 이 저작물의 재이용이나 배포의 경우, 이 저작물에 적용된 이용허락조건을 명확하게 나타내어야 합니다.
- 저작권자로부터 별도의 허가를 받으면 이러한 조건들은 적용되지 않습니다.

저작권법에 따른 이용자의 권리는 위의 내용에 의하여 영향을 받지 않습니다.

이것은 이용허락규약(Legal Code)을 이해하기 쉽게 요약한 것입니다.

Disclaimer

dCollection

Ph.D. Dissertation

Locally Adaptive 2D-3D Registration using Vascular Structure Model for Liver Catheterization

간 조영술을 위한 혈관 모델 기반의 국부 적응 2D-3D 정합 알고리즘 기법 연구

February 2017

Department of Electrical Engineering and Computer Science
College of Engineering
Seoul National University

Jihye Kim

Locally Adaptive 2D-3D Registration using Vascular Structure Model for Liver Catheterization

지도교수 신 영 길

이 논문을 공학박사 학위논문으로 제출함

2016 년 10 월

서울대학교 대학원

전기·컴퓨터 공학부

김 지 혜

김지혜의 공학박사 학위논문을 인준함

2016 년 12 월

위 원 장 김 명 수 (인)

부위원장 신 영 길 (인)

위 원 서 진 욱 (인)

위 원 김 보 형 (인)

위 원 이 정 진 (인)

Abstract

Locally Adaptive 2D-3D Registration using Vascular Structure Model for Liver Catheterization

Jihye Kim
Department of Electrical Engineering and Computer Science and Engineering
College of Engineering
Seoul National University

Two-dimensional-three-dimensional (2D-3D) registration between intra-operative 2D digital subtraction angiography (DSA) and pre-operative 3D computed tomography angiography (CTA) can be used for roadmapping purposes. However, through the projection of 3D vessels, incorrect intersections and overlaps between vessels are produced because of the complex vascular structure, which make it difficult to obtain the correct solution of 2D-3D registration. To overcome these problems, we propose a registration method that selects a suitable part of a 3D vascular structure for a given DSA image and finds the optimized solution to the partial 3D structure. The proposed algorithm can reduce the registration errors because

it restricts the range of the 3D vascular structure for the registration by using only the relevant 3D vessels with the given DSA. To search for the appropriate 3D partial structure, we first construct a tree model of the 3D vascular structure and divide it into several subtrees in accordance with the connectivity. Then, the best matched subtree with the given DSA image is selected using the results from the coarse registration between each subtree and the vessels in the DSA image. Finally, a fine registration is conducted to minimize the difference between the selected subtree and the vessels of the DSA image. In experimental results obtained using 10 clinical datasets, the average distance errors in the case of the proposed method were 2.34 ± 1.94 mm. The proposed algorithm converges faster and produces more correct results than the conventional method in evaluations on patient datasets.

Keywords: 2D-3D registration, Vascular structure model, Subtree, Skeletonization, Catheterization

Student Number: 2013-30228

Contents

Lists of Tables

Lists of Figures

Chapter 1. Introduction

1.1 Background

Interventional radiology (IR) procedures are minimally invasive surgical procedures that inflict less pain and procedure-related morbidity and mortality than conventional open surgery [1]. It provides image-guided diagnosis and treatment of diseases using X-rays, CT, ultrasound, MRI, and other imaging modalities. The images from the modalities aid radiologists in planning interventions and guiding catheter-directed procedures.

Interventional radiology includes various therapies to treat cancers, hypertension, stenosis and other many diseases. In interventional oncology, there are drastic advances over the past three decades. Interventional radiologists can offer an appropriate treatment such as transarterial therapies, percutaneous ablation, and portal vein embolization according to the status of cancer patients [2]. The Transarterial chemoembolization (TACE), one of the most effective intra-arterial treatment for hepatocellular carcinoma, consists of the injection of anticancer drugs into the hepatic artery and the administration of embolizing agents to block the arterial

supply to the tumors [3].

Portal vein embolization (PVE) is the treatment for the patients who needs the resection of the majority of the functional liver mass (up to 70 percent). PVE induces hypertrophy of the future liver remnant before resection by redirecting portal blood to the non-tumor-liver [4]. The portal venous system is accessed percutaneously by the Seldinger technique. A 22-gauge needle is placed into a distal branch of the right portal venous system. Then, a vascular sheath is placed into the right portal vein branch to aid subsequent catheter exchanges. The catheter moves through the portal venous system and the targeted branches are embolized.

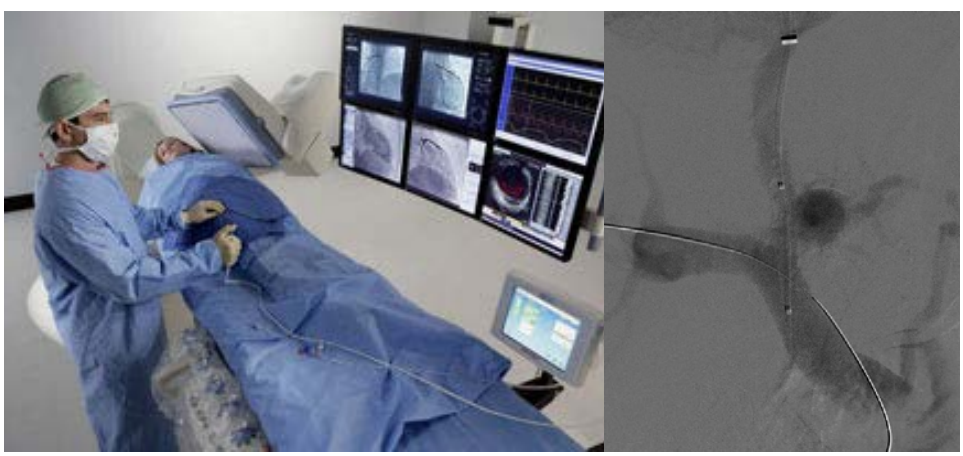

(a) (b)

Figure 1 (a) Demonstration of interventional radiology (Photo by Oakwood Healthcare) (b) Fluoroscopic image of TIPS in progress (Photo by Samir, 2009)

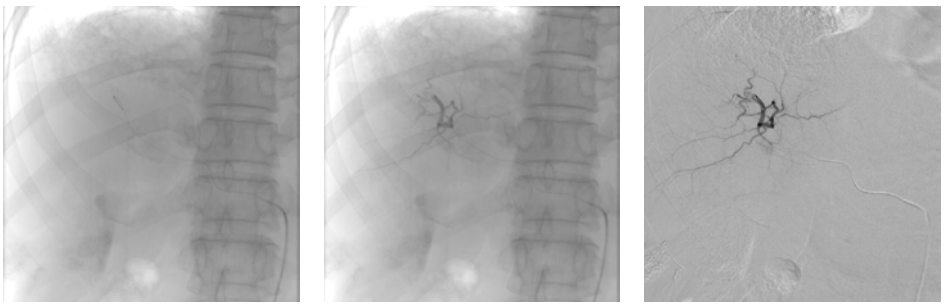

(a) (b) (c)

Figure 2 Conventional angiographic images and DSA image: (a) mask image for DSA (b) targeted angiographic image (c) DSA image obtained by subtracting mask image (a) from (b)

The above procedures should be progressed under fluoroscopic guidance which shows real-time moving images based on X-ray techniques. For example, the PVE procedure is accompanied with a portography which is a radiography performed with an angiographic flush catheter placed within the main portal vein or splenic vein. Anteroposterior and craniocaudal projections are obtained as needed to delineate the portal venous anatomy. Selective left and right portal venography is performed [5].

During intervention, an image guidance is provided by angiography, which is an image technique to visualize blood vessels. Angiography is based on X-ray, but ordinary X-rays doesn't display clearly blood vessels. Hence, blood vessels are highlighted through the use of radio-opaque contrast agents injected via a

catheter [6]. Conventional angiography produces images that contain the contrast-enhanced blood vessels in addition to other tissue and objects such as bone. Digital subtraction angiography (DSA) is a computed-adjusted angiographic sequence with only the blood vessels visible. In DSA, distracting visual images are removed on the screen by first making a mask image before contrast injection and then subtracting the mask from the final image of the vessels under contrast injection.

In addition to two-dimensional (2D) image guidance by conventional angiography or DSA, three-dimensional (3D) computed tomography angiography (CTA) or magnetic resonance angiography (MRA) can aid the procedure. CTA and MRA are less invasive than traditional angiography and has notable diagnostic advantage. [6] Volumetric rendering from CTA or MRA scans allow vessel viewing from multiple, arbitrary angles [7]. The pre-operative CTA or MRA images can be used to plan the intravascular interventions [8] [9]. It is important to recognize and understand the status of anatomy before interventions. In addition, the pre-operative 3D images can aid in guiding catheter-directed procedures by visualizing the 3D vascular structure. The pre-operative 3D images can be viewed in a multiplanar format, which reduces the number of selective catheterizations and angiographic runs. It eventually reduces the amount of iodinated contrast medium used for highlighting vessels

and the fluoroscopy time during interventions when CT images are used as an adjunct to 2D fluoroscopy or DSA [10]. In addition, the 3D imaging information is projected onto the fluoroscopic image, i.e., 3D roadmapping. Figure 3 shows stent-graft deployment for infrarenal abdominal aortic aneurysm using preoperative CTA as a 3D roadmap overlaid on live fluoroscopy. In A, markers are displayed on the renal arteries to be preserved (red and blue circles). One inferior right accessory renal artery was covered and one lower left accessory renal artery embolized before stent-graft deployment to avoid endoleaks. Two guidewires are visible in the projection of the aortic lumen. Next, in B, positioning of the stent-graft using CTA as a roadmap enables a view of the aortic neck without requiring a standard angiogram. Subsequently, deployment of the first two struts of the stent-graft under 3D CTA roadmap control in C. Finally, deployment of the entirety of the aorto-bi-iliac component of the stent-graft.

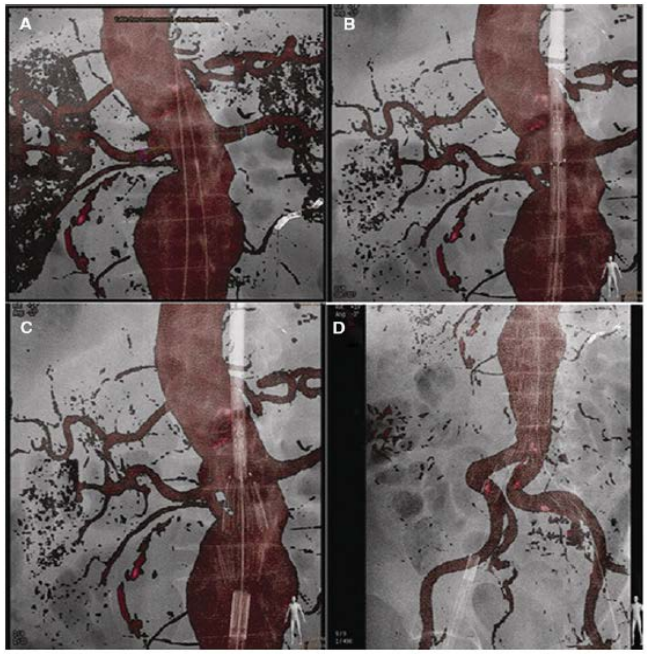

Figure 3 Stent-graft deployment for infrarenal abdominal aortic aneurysm using preoperative CTA as a 3D roadmap overlaid on live fluoroscopy [11]

1.2 Problem statement

Since 2D angiography images scan the limited areas near the catheter, it is difficult to figure out the overall structure of the vasculature and the location of the catheter. Moreover, geometric information is lost through projection, which makes it difficult to recognize the connectivity between vessels. Computed tomography angiography

(CTA) data can compensate for these limitations of 2D angiography because they provide the overall 3D vascular structure. Hence, it can be used for making a roadmap that shows the currently traversed vessel and the distal vessel tree.

However, to utilize the 3D CTA data effectively, an accurate registration between 2D angiography and 3D CTA images is needed. The 3D vascular structure is overlaid on 2D angiographic images during the procedures. The 3D roadmap gives interventional radiologists useful information only when the 3D vascular structure is projected with the similar direction and angulation as the 2D angiographic images are produced. Therefore, the registration process is needed to find the appropriate transformation factors matching 3D CTA data to 2D angiographic image.

In this thesis, we propose a novel 2D−3D registration algorithm between DSA image and 3D CTA scans with high accuracy by finding an appropriate parts from 3D vascular structure and computing transformation factors only with a partial structure related with a given DSA image.

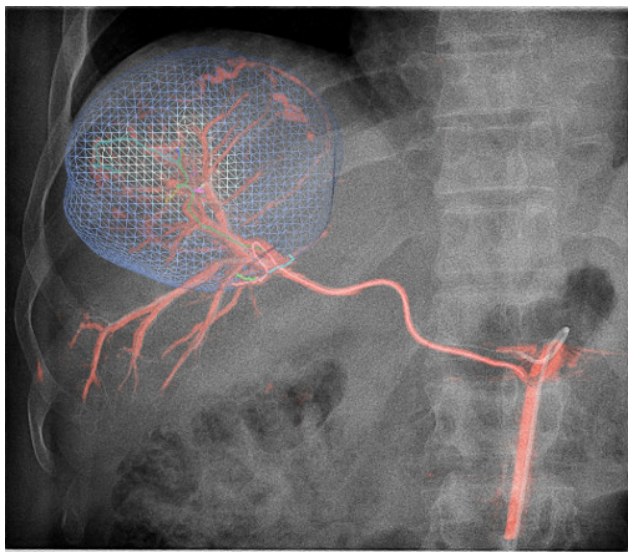

Figure 4 The 3D roadmap is superimposed on the live fluoroscopy [12]. The gray scale background is the fluoroscopy, the red colored overlay is the arterial tree and the blur colored overlay represents the targeted liver tumor

1.3 Main contributions

We propose a method that finds a currently traversed area in a 3D vascular structure for a given DSA image and registers the 3D vessels to the 2D vessels on the DSA by using the subtree structure of the 3D vessels. We improve the accuracy of the registration by dividing a 3D vascular tree model into several subtrees and using only one of the subtrees in the registration process. The 3D vascular structure is very complex, and therefore, the projection of the entire

structure causes a considerable number of overlapped vessels and incorrect intersection points. This leads to a false local minima in the registration process, particularly when a DSA image shows only a part of the vascular structure. We overcome these problems by dividing the 3D structure into several subtrees and using only the relevant part of the given DSA image. To search for the appropriate part of the DSA image, we first construct a tree model of the 3D vascular structure considering their connectivity and divide it into several subtrees. Subsequently, the best matched subtree for the given DSA image is selected according to the dissimilarity measure from the coarse registration between each subtree and the DSA image. Finally, fine registration is conducted for the selected subtree by using a distance metric. Then, by restricting the range for the registration process, we obtain better convergence and higher accuracy than the registration using all the 3D vessels.

The proposed method consists of four main steps, as shown in Figure 5. First, we analyze the pre-operative 3D CTA and the intra-operative 2D DSA. From the 3D CTA, a 3D vascular structural model is constructed and divided into several subtrees. During intervention, a 2D vessel centerline is computed from the 2D DSA. Next, the best matched subtree for a 2D vessel centerline is selected by comparing the dissimilarity among the subtrees. Finally, fine registration is conducted for the selected subtree.

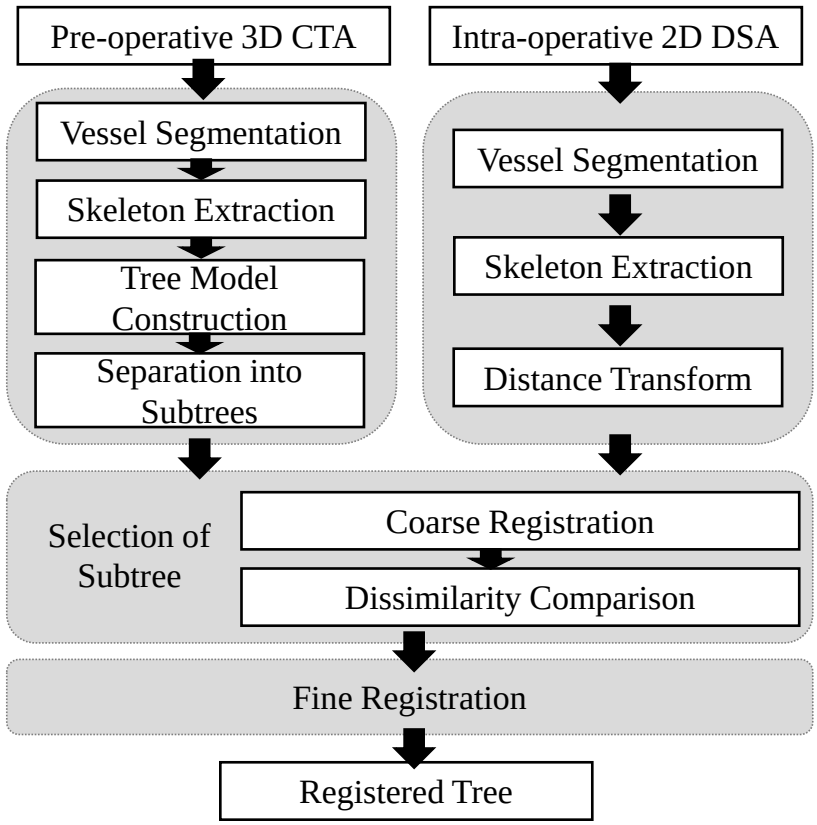

Figure 5 Process of the proposed 2D−3D registration

1.4 Contents organization

The remainder of this thesis is organized as follows: The next section introduces the previous works of 2D−3D registration methods. Section 3 describes a method of constructing the 3D vascular structure model. Section 4 explains the locally adaptive registration

algorithm using the 3D model. Section 5 discusses the experimental results and is followed by Section 6 that presents the conclusion.

Chapter 2. Related Works

2.1 Overview

The registration methods can be classified according to nine criteria: dimensionality, nature of registration basis, nature of transformation, domain of transformation, interaction, optimization procedure, modalities, subject, and object. [13] We focused on 2D-3D registration for endovascular interventions and categorized the registration methods into 3 groups according to the object or application: head, cardiac, and liver, which are most actively studied areas in vascular image registration. Each group is classified into rigid and non-rigid registration by the nature of transformation. Most registration algorithms for neurovascular focus on only rigid transformation because of the non-deformable property of head. On the contrary, many researches in cardiac application suggests rigid and non-rigid registration methods because handling respiratory motions is very important issues in the cardiac application.

Classification for medical registration methods

Ⅰ. Dimensionality
- a. Spatial dimensions only:
  - 1. 2D/2D
  - 2. 2D/3D
  - 3. 3D/3D
- b. Time series (more than two images), with spatial dimensions:
  - 1. 2D/2D
  - 2. 2D/3D
  - 3. 3D/3D

Ⅱ. Nature of registration basis
- a. Extrinsic
  - 1. Invasive
    - A. Stereotactic frame
    - B. Fiducials (screw markers)
  - 2. Non-invasive
    - A. Mould, frame, dental adapter etc.
    - B. Fiducials (skin markers)
- b. Intrinsic
  - 1. Landmark based
    - A. Anatomical
    - B. Geometrical
  - 2. Segmentation based
    - A. Rigid models (points, curves, surfaces)
    - B. Deformable models (snakes, nets)
  - 3. Voxel property based
    - A. Reduction to scalars/vectors (moments, principal axes)
    - B. Using full image content
- c. Non-image based (calibrated coordinate systems)

Ⅲ. Nature of transformation
- a. Rigid
- b. Affine
- c. Projective
- d. Curved

Ⅳ. Domain of transformation
- a. Local
- b. Global

Ⅴ. Interaction
- a. Interactive
  - 1. Initialization supplied
  - 2. No initialization supplied
- b. Semi-automatic
  - 1. User initializing
  - 2. User steering/correcting
  - 3. Both
- c. Automatic

Ⅵ. Optimization procedure
- a. Parameters computed
- b. Parameters searched for

Ⅶ. Modalities involved
- a. Monomodal
  - 1. Autoradiographic
  - 2. Ct or CTA
  - 3. MR
  - 4. PET
  - 5. Portal
  - 6. SPECT
  - 7. US
  - 8.Video
  - 9. X-ray or DSA
- b. Multimodal
  - 1. CT-MR
  - 2. CT-PET
  - 3. CT-SPECT
  - 4. DSA-MR
  - 5. PET-MR
  - 6. PET-US
  - 7. SPECT-MR
  - 8. SPECT-US
  - 9. TMS-MR
  - 10. US-CT
  - 11. US-MR
  - 12. X-ray-CT
  - 13. X-ray-MR
  - 14. X-ray-portal
  - 15. X-ray-US
  - 16. Video-CT
  - 17. Video-MR
- c. Modality to model
  - 1. CT
  - 2. MR
  - 3. SPECT
  - 4. X-ray
- d. Patient to modality
  - 1. CT
  - 2. MR
  - 3. PET
  - 4. Portal
  - 5. X-ray

Ⅷ. Subject
- a. Intrasubject
- b. Intersubject
- c. Atlas

Ⅸ. Object
- a. Head
  - 1. Brain or skull
  - 2. Eye
  - 3. Dental
- b. Thorax
  - 1. Entire
  - 2. Cardiac
  - 3. Breast
- c. Abdomen
  - 1. General
  - 2. Kidney
  - 3. Liver
- d. Pelvis and perineum
- e. Limbs
  - 1. General
  - 2. Femur
  - 3. Humerus
  - 4. Hand
- f. Spine and vertebrae

Figure 6 Registration criterion description from [13]

Markelj et al. [14] has provided an extensive review of the existing 2D-3D registration methods. Matl et al. has focused on vascular image registration [15] and they provided a web-based interactive app which visualized the classification of vascular image registration.

2.1.1 Definitions

A registration can be defined based on geometrical transformations, which are mappings of points from the space X of one view to the space Y of a second view. [16] The transformation $\mathcal{T}$ applied to a point X represented by the column vector $\mathbf{x}$ produces a transformed point $\mathbf{x}'$,

$$\mathbf{x}' = \mathcal{T}(\mathbf{x}).$$

If the point $\mathbf{y}$ in Y corresponds to $\mathbf{x}$, then a successful registration will make $\mathbf{x}'$ equal, or approximately equal, to $\mathbf{y}$. Any nonzero displacement $\mathcal{T}(\mathbf{x}) - \mathbf{y}$ is a registration error.

We define a 2D-3D registration as a registration mapping 3D scans into 2D X-ray images. Images obtained by X-ray projection are two-dimensional views of three-dimensional objects by projecting X-rays from a three-dimensional scene onto a two-dimensional plane. Therefore, to define a registration between 2D X-

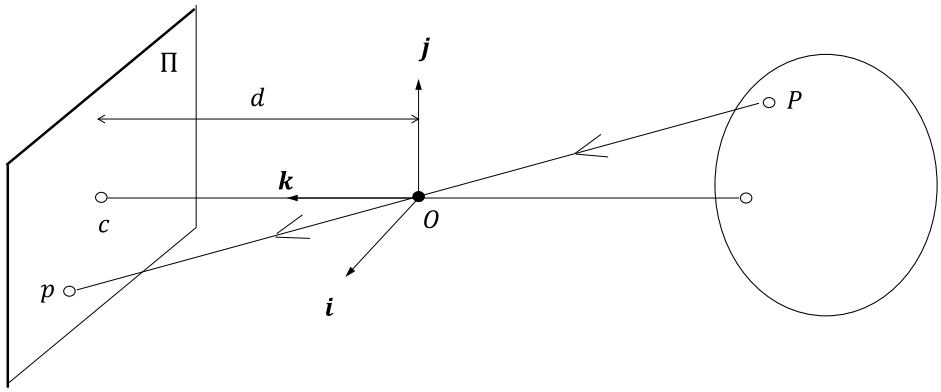

Figure 7 The perspective projection equations are derived from the collinearity of the point $\boldsymbol{P}$, its image $\boldsymbol{p}$, and the pinhole O [17]

ray images and 3D scans, the transformation is defined as a perspective transformations based on a pinhole camera model as shown in Figure 7. A ray from a point P in the world scene is projected through the pinhole O onto an image plane Π.

The perspective projection is explained in the following equation using homogenous coordinates [17]:

$$\boldsymbol{p} = \frac{1}{Z}\mathcal{M}\boldsymbol{P}$$

where $\mathcal{M}$ is a 3×4 homogeneous perspective projection matrix, $\boldsymbol{P} = (X, Y, Z, 1)^{\mathrm{T}}$ is a coordinate vector of a point P in world coordinate system and $\boldsymbol{p} = (\mathrm{x}, \mathrm{y}, 1)^{\mathrm{T}}$ is a coordinate vector of its image p in the image plane Π. (Figure 7)

The perspective projection parameters can be divided into the intrinsic parameters and extrinsic parameters. The intrinsic

parameters relate the camera's coordinate system to the idealized coordinate system and the extrinsic parameters relate the camera's coordinate system to a fixed world coordinate system. Hence, the perspective projection matrix $\mathcal{M}$ is defined as follows:

$$\mathcal{M} = \mathcal{K}(\mathcal{R} \mid t)$$

where $\mathcal{K}$ is the calibration matrix which consists of the intrinsic parameters of the camera, $\mathcal{R}$ is a rotation matrix and t is a translation vector. Since a rotation matrix $\mathcal{R}$ is defined by three independent parameters and t consists of three parameters, we obtain a set of six extrinsic parameters that define the position and orientation of the camera relative to the world coordinate frame.

The intrinsic parameters can be obtained by acquiring images of a suitable calibration object, or they can be estimated using the source to image distance (SID) and the field of view (FOV) obtained from the X-ray set and assuming that the center of the image intensifier is exactly perpendicular to the X-ray source. [18] Since most X-ray set provide information for the latter approach, the calibration matrix K can be assumed to be given before the registration process.

Therefore, many researches of 2D-3D registration aim to find appropriate extrinsic parameters, $\mathcal{R}$ and t, which is a rigid registration. Then, a rigid 2D-3D registration algorithm finds appropriate $\mathcal{R}$ and t which satisfy the following equation:

$$\mathcal{T}' = \arg\min_{\mathcal{T}} \mathcal{E}$$

,where $\mathcal{T}(P) = \mathcal{R}P + t$ and $\mathcal{E}$ denotes an energy function or cost function of registration, which represents a registration error.

To improve the accuracy of a registration method, a non-rigid registration algorithm can be introduced, which deals with local deformations while a rigid registration consider only a global transformation. In non-rigid registration, the transformation is defined as a set of displacement vectors. Non-rigid registration process can reduce registration errors by compensating local deformation when the global deformation is fixed.

2.1.2 Intensity-based and feature-based registration

Image registration can be classified into intensity-based and feature-based approaches [19]. Feature-based 2D-3D registration methods finds the transformation that minimizes the distances between 3D features and corresponding 2D features. On the contrary, intensity-based 2D-3D registration methods use information contained in voxels and pixels of 3D and 2D images, respectively [14]. Figure 8 shows the geometrical setup of image-based and feature-based 2D-3D registration.

In intensity-based 2D-3D registration, the similarity measure is

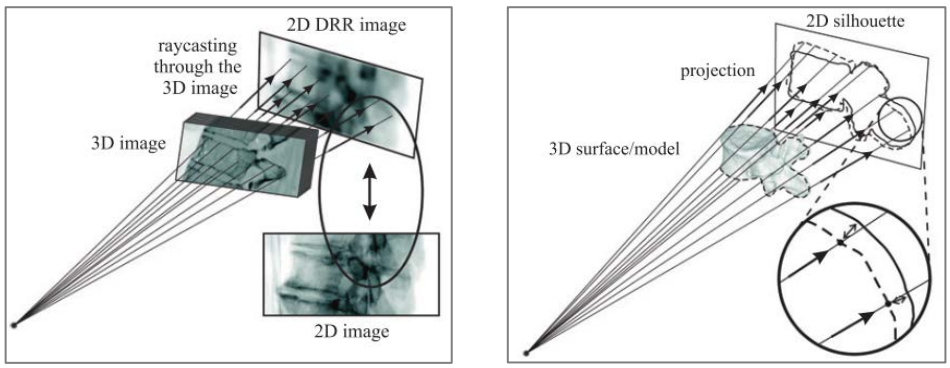

(a) (b)

Figure 8 Overview of image-based (a) and Feature-based (b) 2D-3D registration [14]

calculated using pixel-wise comparison. To achieve dimensional correspondence between 2D and 3D images, most intensity-based 2D-3D registration methods use simulated X-ray projection images called digitally reconstructed radiographs (DRRs). These are produces from CT images using ray-casting [20]. The 2D-3D registration iteratively optimizes the similarity measure calculated between 2D image and a DRR produced from CT images with the current transformation. Intensity-based registration needs no feature extraction or segmentation, and therefore, it does not suffer from segmentation errors. However, the DRR generation requires the high computational cost, which makes the registration slow.

In contrast to intensity-based registration, feature-based 2D-3D registration methods finds the transformation that minimizes the

distances between 3D features and corresponding 2D features. The features can be points, curves, or surface in accordance with applications. Therefore, feature-based registration methods should accompany suitable segmentation algorithm to extract features. The accuracy of segmentation has a decisive effect on the accuracy of a registration. In contrast to intensity-based registration, feature-based registration processes only features, not whole image. Hence, the computation cost for registration is relatively low.

2.2 Neurovascular applications

Registration methods for neurovascular applications can be categorized into 3 groups: intensity-based, feature-based and hybrid methods. Most feature-based registrations define the cost function as the Euclidean distance between center points which are obtained from 3D scans and 2D images, respectively. [21], [22], [23], [24]. In [25], the distance function is defined as the Euclidean distance function which takes into account both for the 2D spatial distance and the difference in tangent orientations.

Intensity-based registration methods find an appropriate transformation which maximizes the similarity between a 2D image

and a projection image. Kerrien et al. [26] and Hentschke et al. [27] used normalized cross correlation in order to compute the similarity between a DSA image and a Maximum Intensity Projection (MIP) of the 3D scans. Hipwell et al. [28] compared the performance of the following six measures to quantify the similarity between X-ray image and DRR which is computed from 3D MRA: normalized cross correlation [29], gradient correlation [30], entropy of the difference image [31], mutual information [32], pattern intensity [33], and gradient difference [34]. The most accurate and robust registrations were obtained using pattern intensity, gradient difference and gradient correlation. Mitrović et al. [35] split the registration process into two step. The initial step found in-plane translation parameters by machine-based or template matching and the final step evaluated four intensity-based 3D-2D registration methods.

McLaughlin et al. compared an intensity-based algorithm and a feature-based algorithm [23] [24] [36]. In [36], they evaluated an intensity-based algorithm using the gradient difference and an iterative closest point-based algorithm. In phantom studies, the ICP-based algorithm was more reliable, but with more complicated clinical data, the gradient difference algorithm was more robust.

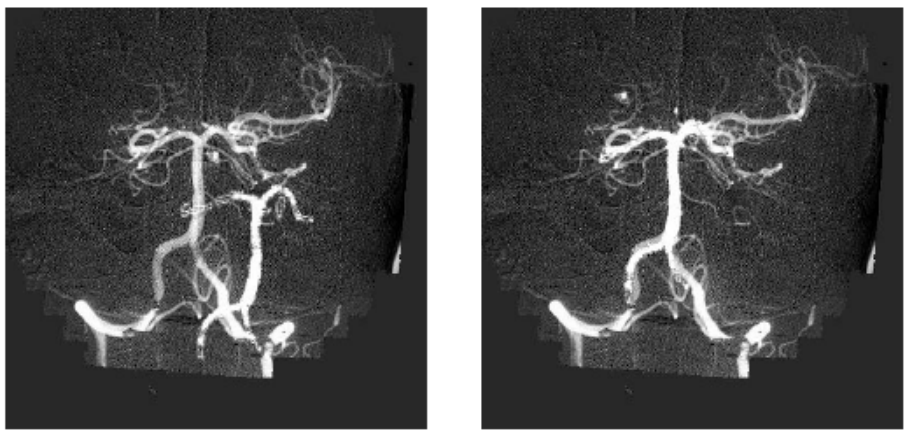

Figure 9 The projection of the 3D MRA segment projected on the DSA image before (left) and after (right) registration [38]

Hybrid approach uses both the intensity information and the extracted features. Chan et al. [37] and Lau et al. [38] segmented 3D vascular structure from 3D volume and extracted the skeleton. Then, a binary volume was reconstructed by the set of spheres with the centers on the skeleton points and radii which represents distance to the closest boundary. A projected image was generated by the projection of spheres and the similarity between a DSA and a projection image of the binary volume is computed using the sum of squared differences.

Florin et al. [39] and Sundar et al. [40] defined the similarity

measure using the distance transform. The difference between the 3D scans and the 2D image is computed by the distance between the projection of the extracted skeleton from 3D scans and the skeleton extracted from 2D image. To approximate the distance, the distance transform for the 2D skeleton is computed. Then, the distance is defined as the sum of values in the distance transform at the projected points of 3D skeleton.

Mitrović et al. [41] [42] matched a 3D vasculature model to intensity gradients of 2D image. The skeleton is extracted from 3D volume and the orientation and radii of the points on the skeleton is obtained using Hessian analysis. The 3D skeleton is projected onto 2D image and the orientation in the 2D plane is computed by the projection parameters. Subsequently, the similarity is defined based on the orientation and the intensity gradients of 2D image.

2.3 Liver applications

Registration algorithm for liver applications follow the strategy of minimizing the distance between the vessels of a 2D image and the projection of 3D vessels. Groher *et al.* [43] detects the branching points of the thickest 2D and 3D vessels as root nodes and finds the

x-y translation in the initialization step. Subsequently, they optimizes the transformation parameters by using the difference between centerlines and the projection of 3D vessels. Further, they use topological information such as the degree of bifurcation points in order to enhance the accuracy of the registration algorithm. Jomier *et al.* [44] proposed the sum of the Gaussian-blurred intensity values in the 2D image at the projected points of 3D model as a registration metric. Groher et al. improved the registration accuracy using a probability map [45]. They computed a probability for each pixel to be registered using vesselness measure and error with corresponding 3D points. Subsequently, they extracted 2D vessels based on the probability map and evaluated the similarity only for points on 2D vessels.

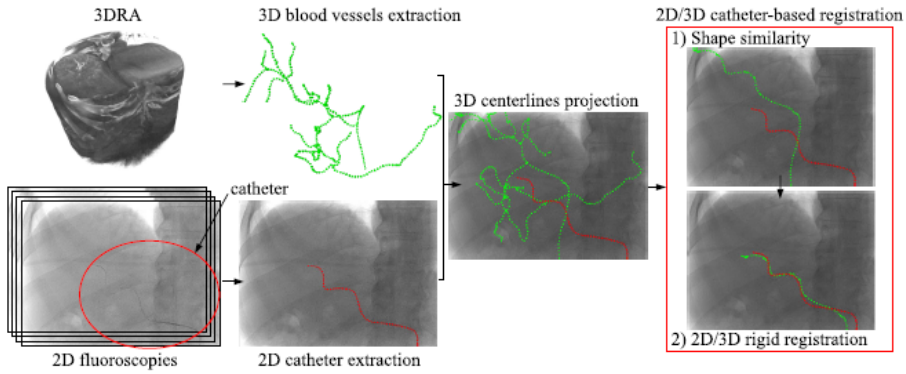

Figure 10 Global overview of Ambrosini's registration process: vessels/catheter extraction and 2D/3D registration

Groher et al. proposed non-rigid registration algorithm for liver applications [46] [47]. In [46], Groher et al. found a set of 3D displacement vectors which minimize the distance between the 2D points and corresponding projected 3D points with two regularization terms, the length preservation of vessel structures and smoothness of deformation. [47] defined data term with radii of centerline points of 3D volume, which leads to decrease the runtime compared to [46] with maintaining similar accuracy.

Although these algorithms show a high accuracy and a robust convergence, they assume that the contrasted vessels in DSA have a similar range to that of the 3D vessels from CTA scans. However, in

the liver application, a contrast medium is injected, and only the limited areas near the catheter are displayed in the angiography images while the catheter is moved through the vascular structure. Ambrosini *et al.* [48] overcame this problem by selecting an appropriate leaf vessel centerline from the 3D vascular structure according to the shape similarity with the catheter centerline. This method selects the appropriate vessel centerline in most cases and shows a high accuracy in the registration results. However, it fails to find a correct solution when a small part of the catheter is visible on the image or the shape of the catheter does not have a predominant feature.

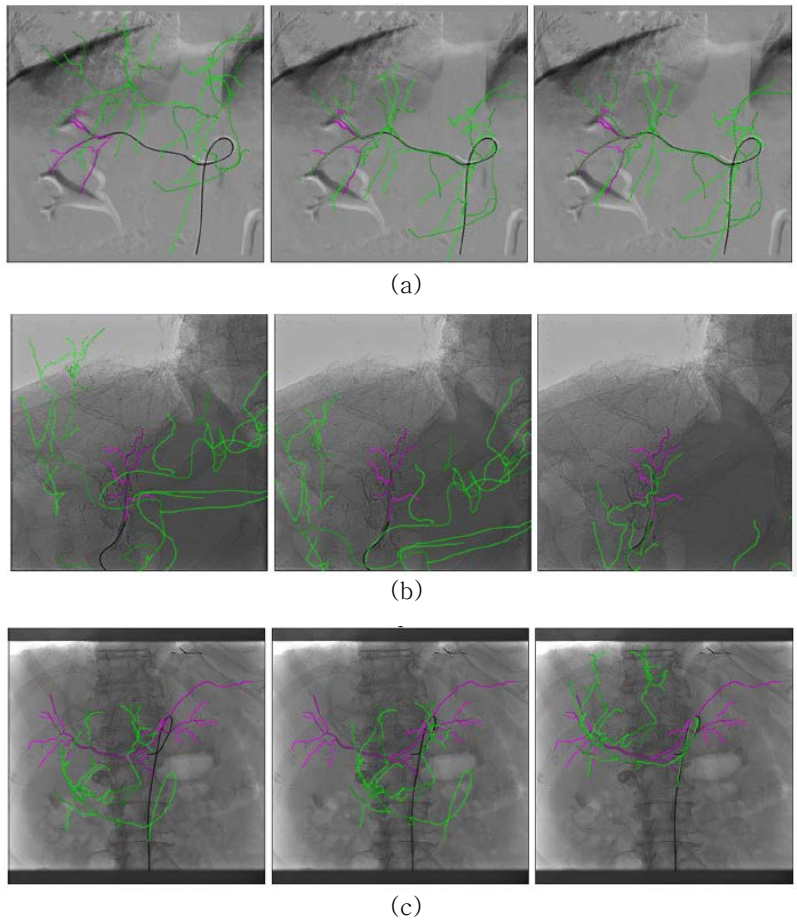

Figure 11 Results of Ambrosini's registration algorithm: Projection of the 3DRA blood vessel (in green) with the catheter (in black) and the contrast agent (in purple). Initial position (left). Registered position with Powell (middle). Registered position with brute force (right). (a) The registration is correct. Here the catheter is long enough to give information. (b) The catheter part is too short. Powell registered with a good distance metric but the result is wrong. Brute force is correct. (c) As a long part of the aorta is missing in the 3DRA, Powell stops in a local minimum while brute force is more exhaustive and reach the global minimum

2.4 Cardiac applications

2.4.1 Rigid registration

A registration can be defined based on geometrical transformations, which are mappings of points Registration methods for neurovascular applications can

In cardiac application, it is important to deal with breathing motion. Electrocardiogram (ECG) gating is used to obtain the X-ray image at the desired cardiac phase, for example, at end diastole which is the most quiescent phase of the cardiac cycle [49].

Pre-operative 3D data is reconstructed during mid-to-end diastolic phase, which coronary artery displacement is relatively small. Then, a single frame is selected from intra-operative fluoroscopy sequence by matching the acquisition cardiac phase of the 3D volume using ECG signal. [50] Corresponding acquisition cardiac phase from the CT volume is expressed using a percentage interval between two consecutives R-wave (R-R interval) from the QRS complex. The QRS peak is automatically detected using the first and second derivative of a curve fitted onto the ECG signal, to identify

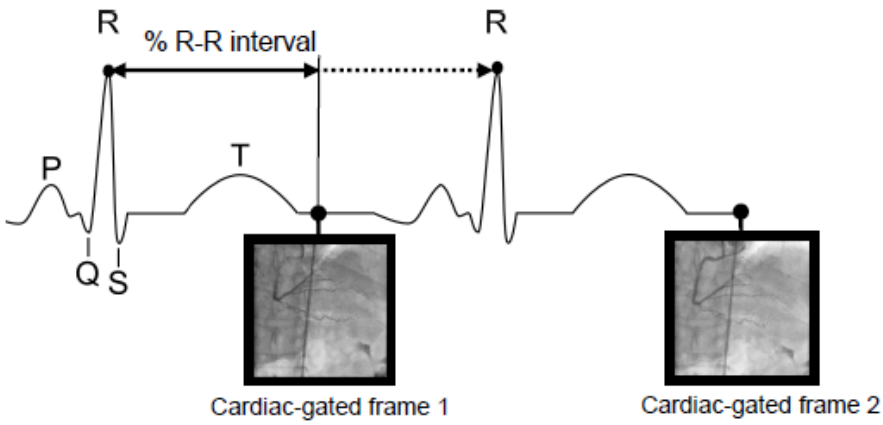

Figure 12 Cardiac gating using the ECG signal [50]. The percentage from the R-R interval of the ECG signal is used to synchronize the current cardiac phase with fluoroscopy with the MSCT acquisition. Remaining motion is due to the respiratory functions of the patient.

inflexion points corresponding to the QRS peak. From the QRS peak detected, the RR-interval is matched with the RR-interval store in the DICOM header of the CT acquisition. Therefore, when we assume that a 3D volume and a 2D image of 2D-3D registration process are obtained by the above explained phase alignment, the registration of cardiac application can be defined as a registration between a single 3D volume and a single 2D image.

Many registration methods of cardiac application were presented for a 3D volume and a 2D image with the phase alignment [50] [51]

[52] [53] [54] [55] [56]. Similar to other applications, the registration methods compute the appropriate transformation to match a 3D volume and a 2D image by minimizing the distance between the extracted 2D vessel skeleton and the projection of the extracted 3D vessel skeleton. Ruijters et al. [53] used a distance-based cost function using distance transform. A distance transform is computed for the projected 3D data and the similarity is defined of the sum of all pixel values of the distance transform with weighted by the vesselness measure. [57]

Dibildox et al. [55] converts the 2D-3D registration into 3D-3D registration problem by reconstructing 3D vessel centerline model from the biplane X-ray images using an adaptive 3D epipolar geometry algorithm. Then, the extracted 3D centerlines from 3D CTA and the reconstructed 3D vessel centerline model are represented as Gaussian mixture models and the distance measure for the registration is defined as the distance between two Gaussian mixture models.

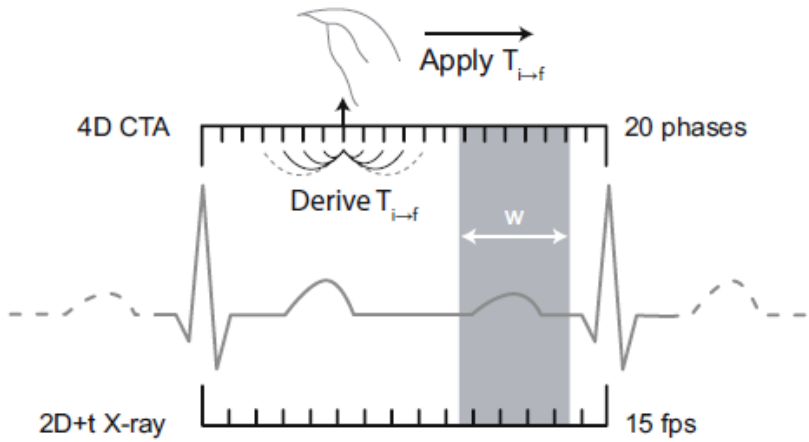

Figure 13 Metz's 4D model creation and 2D+t/3D+t registration approach [58]

Metz et al. constructed 4D (3D+t) coronary models and registers the model to X-ray image sequence [58] [59]. Instead of matching 3D and 2D data at one time point, they match multiple sequential time-points of the 4D coronary model to multiple sequential X-ray images simultaneously. First, a 3D centerline model of the coronary arteries is derived from a phase in the cardiac cycle with minimal motion. Deformation of the coronary arteries is subsequently derived from the 4D CTA data by a non-rigid registration. Finally, the derived 4D model is applied in a 2D+t/3D+t registration procedure which minimizes normalized cross correlation between X-ray images

and DRRs of the coronary model.

2.4.2 Non-rigid registration

The coronary motion is a complex combination of rigid and non-rigid deformations caused by both cardiac and respiratory activities. To overcome the problems caused by the dynamic coronary motion, non-rigid registration algorithms were proposed for cardiac applications [60] [61] [62] [63].

Rivest-Hénault et al. [61] proposed a non-rigid registration algorithm which consists of global alignment and local non-rigid registration. In global alignment, an affine transformation is computed to minimize the distance between 2D centerlines and the projection of 3D vessel skeleton. The distance is defined as the sum of pixel values of distance transform at the projected location of 3D skeleton. Then, a local non-rigid registration compensate local deformations with a distance measure and regularization constraints that maintain the smoothness and a certain degree of rigidity of the vessels.

Hadida et al. [62] enforces temporal consistency using a Hidden Markov Model and considers multiple hypotheses simultaneously

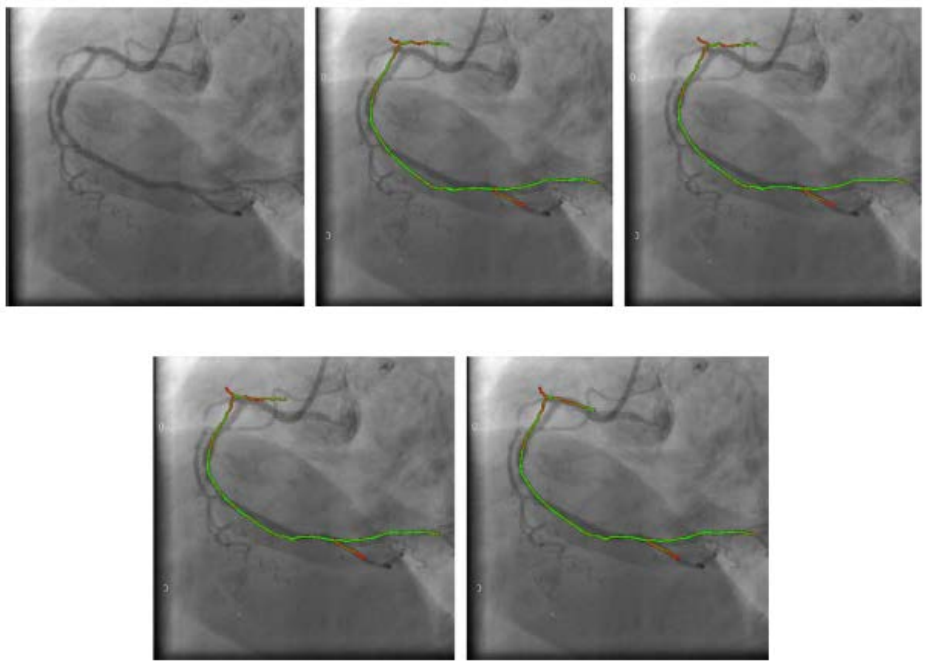

Figure 14 Progression of a non-rigid registration [61]. (First row) From left to right: sample input image, and position of the centerline after 0 and 50 iterations. (Second row) From left to right: position of the centerline after 350 and 1200 iterations.

during the optimization process using particle filtering [64]. Kim et al. [63] used the thin plate spline robust point matching with energy function which consists of distance term, smoothness term and robustness control term.

Chapter 3. 3D Vascular Structure Model

3D vascular structure model is constructed from pre-operative CTA data. The constructed model is used for 2D-3D registration process during intervention. We segment 3D vessels from pre-operative CTA data, and extract skeletons from segmented 3D vessels. The skeletons are converted into a tree model, and finally, the tree model is divided into several subtrees.

By constructing model before intervention, we don't need to analyze 3D data during intervention, which can reduce the computation time for 2D-3D registration.

The model should correctly represent the connectivity between vessels because it decides the accuracy of the registration process. Therefore, we apply the skeletonization algorithm which computes the subvoxel precise skeleton using the fast marching method [65]. Moreover, we separate a tree model into several subtrees considering their connectivity.

3.1 Vessel segmentation

To construct a vascular structure model, we first segment 3D vessels from CTA. In this section, we introduce vessel segmentation algorithm, and then, explain our segmentation algorithm.

3.1.1 Overview

The vessel segmentation methods can be classified as follows: Region-growing algorithms, active-contours and centerline-based approaches. [66]

Region-growing approaches incrementally segment an object by recruiting neighboring voxels based on some inclusion criteria from seed points or regions located inside a vessel. Region-growing approaches are widely applied in many segmentation methods because of their computational efficiency and simplicity.

Active contours are popular techniques of image segmentation. Active contours evolve an interface through external forces derived from the image and internal forcers constraining the contour geometry and its regularity. [67] They can be defined by the

integration of various internal and external forces.

Centerline-based techniques focus on directly extracting the vessel centerline while the region-growing and active contour methods aim at explicitly and directly detecting vessel contours. They improve the robustness of segmentation algorithm by computing the localization of the center of the vessel, the estimation of its direction and scale. In most cases, a rough volume segmentation can be obtained directly by enriching the centerline with the underlying scale information.

The centerline can be extracted by direct centerline tracking which starts from a given seed point and iteratively find successive centerline positions. On the other hand, the centerline extraction problem can be formulated as minimal path optimization between start and end points. The cost metric is designed to estimate centerline locations and a popular feature for the cost metric is the Hessian-based vesselness measure [57]. The metric is used in [68], [69], [70] and many other centerline extraction methods.

3.1.2 Vesselness filter

The Hessian-based vesselness measure is a popular metric for vessel segmentation. The measure was proposed from [57], [71] and [72]. The measure proposed by Frangi et al. [57] are used in our vessel segmentation method.

The vesselness measure for each pixel is computed to represent a possibility that a pixel can be on a tubular shaped structure. Therefore, the vesselness filter is appropriate for detecting tubular shapes such as vessels.

The vesselness measure is obtained with eigenvalues of Hessian matrix for several scales. The second derivative of a Gaussian kernel at scale s generates a probe kernel that measures the contrast between the regions inside and outside the range $(-s, s)$ in the direction of the derivative. (Figure 15, left) The eigenvalue decomposition extracts three orthonormal directions which are invariant up to a scaling factor when mapped by the Hessian matrix. In particular, a spherical neighborhood centered at $\mathbf{x}_o$ with radius 1 will be mapped by Hessian matrix onto an ellipsoid whose axes are along the directions given by the eigenvectors of the Hessian and the

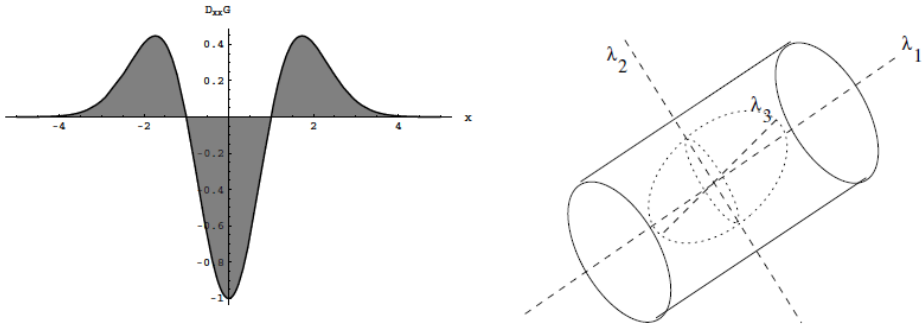

Figure 15 (Left) The second order derivative of a Gaussian kernel probes inside/outside contrast of the range (−s,s). (Right) The second order ellipsoid describes the local principal directions of curvature

corresponding axis' semi−lengths are the magnitudes of the respective eigenvalues. (Figure 15, right)

If λ_k denotes the eigenvalue with the k−th smallest magnitude ($|\lambda_1| \leq |\lambda_2| \leq |\lambda_3|$), we can derive two geometric ratios based on the second order ellipsoid. The first ratio accounts for the deviation from a blob−like structure:

$$R_B = \frac{\text{Volume}/(\frac{4\pi}{3})}{\left(\frac{\text{Largest Cross Section Area}}{\pi}\right)^{3/2}} = \frac{|\lambda_1|}{\sqrt{|\lambda_2\lambda_3|}}$$

The second ratio is essential to distinguish between plate−like and line−like structures:

$$R_A = \frac{(\text{Largest Cross Section Area})/\pi}{(\text{Largest Axis Semi} - \text{length})^2} = \frac{|\lambda_2|}{|\lambda_3|}$$

The second ratio will be zero only in line-like structures. In addition to the two geometric ratios, the measure of second order structureness S is defined for extracting background pixels which has small derivatives, and thus small eigenvalues:

$$S = \sqrt{\sum_{j \le D} \lambda_j^2}$$

Where D is the dimension of the image. Then, the vesselness filter for scale s can be defined as the combination of two ratios and second order structureness. The response of the filter is maximal only if all three criteria are fulfilled. The vesselness filter for scale s can be defined as follows:

$$V(s) = \begin{cases} 0 & \text{, if } \lambda_2 > 0 \text{ or } \lambda_3 > 0 \\ \left(1 - \exp\left(-\frac{{R_A}^2}{2\alpha^2}\right)\right) \exp\left(-\frac{{R_B}^2}{2\beta^2}\right) \left(1 - \exp\left(-\frac{S^2}{2c^2}\right)\right) & \text{, otherwise} \end{cases}$$

where α, β, and c denote the thresholds to control the sensitivity of the filter to the measures R_A, R_B, and S, respectively.

The vesselness measure is calculated at different scales, and the final estimate of vesselness is obtained as follows:

$$V(x) = \max_{s_{min} \le s \le s_{max}} V(s, x).$$

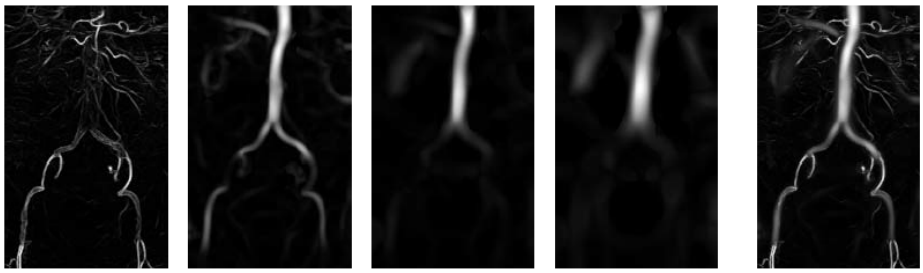

Figure 16 Maximum intensity projections of the vesselness for MRA image at four scales. The first four images show the vesselness obtained at increasing scales. The last image is the result after the scale selection procedure.

Figure 16 shows the result obtained by computing the vessleness measure for 3D aortoiliac MRA dataset. The last image yields the small and large vessels can be detected using the vesselness measure.

3.1.3 Vessel segmentation

In this thesis, we apply the region-growing approach for vessel segmentation and use the vesselness measure as the metric to find vessel candidate area.

To extract vascular structure from a CTA scan, first we compute the vesselness measure for each voxel of the CTA scan.

Subsequently, we binarize the volume data using a threshold for the vesselness measure. We set the threshold to 0.05 for the CTA scan. Finally, we perform a 3D connected component analysis and detect the largest connected component as a 3D vessel. compared the detection accuracy results.

3.2 Skeleton extraction

3.2.1 Overview

The skeleton, or medial axis of an object is the set of all points having more than one closest point on the object' s boundary. It was introduced by Blum [73] for modeling new descriptors of shape. In 2D−3D vessel registration, the skeletons of vessels are extracted from segmented vessels, and used as features to compute the similarity between 2D and 3D vessels.

The thinning is a frequently used techniques to construct an approximation of skeleton. It erodes the surface voxels of object until the skeleton remains. To preserve topology of the original structure, thinning technique removes only simple points which doesn't change

the topology when deleted [74]. Davies [75] and Lee [76] proposed efficient methods to detect simple points. Selle et al. [77] used topology-preserving thinning algorithm to extract skeleton from segmented vessels. In addition, to remove irrelevant skeleton lines, they apply thresholding with steepest gradient for the distance to the boundary.

Gülsün et al. extract skeleton from CTA or MRA data using graph-based optimization algorithm [78]. They designed medialness filters with respect circular/elliptic vessel cross-section property and constructed the full vessel skeleton tree using minimum-cost path detection with a saliency measure computed from length and radius information.

3.2.2 Skeleton extraction based on fast marching method

We apply an automatic skeletonization algorithm based on fast marching method proposed by Van Uitert et al. [65] to extract the skeleton from the segmented vessels. Although there are many algorithms for computing the skeletons [77], [78], we apply the method proposed in [65] because it is suitable for constructing a graph model. The skeleton computed by this method consists of

several branches, each of which can be defined as a node of a graph where a branch is a set of connected voxels on the skeleton. Further, the connectivity between branches is decided during the skeletonization, and therefore, it is easy to construct the tree model hierarchically.

Van Uitert et al. constructs the skeleton of vessels using fast marching method. When we solve level set problem which evolves only outwards and positive evolution speed, it can be represented by an Eikonal equation:

$$|\nabla T|F = 1, \qquad T = 0 \text{ on } \Gamma,$$

where T denotes the arrival time function, F represents the speed of the evolution function, and Γ stands for the initial isosurface at time zero.

An efficient method to numerically evaluate the solution of the equation is the fast marching method. [79] The algorithm processes the voxels in a sorted order based on increasing values of T. The discretization of an Eikonal equation is given by

$$\max\left(D_{i,j,k}^{-x}, 0\right)^2 + \min\left(D_{i,j,k}^{+x}, 0\right)^2 + \max\left(D_{i,j,k}^{-y}, 0\right)^2 + \min\left(D_{i,j,k}^{+y}, 0\right)^2 + \max\left(D_{i,j,k}^{-z}, 0\right)^2 \min\left(D_{i,j,k}^{+z}, 0\right)^2 = F_{i,j,k}^{-2}$$

where $D_{i,j,k}^{-x}$ and $D_{i,j,k}^{+x}$ are values resulting from backward and

forward difference calculations at point (i, j, k) respectively.

The main steps of the skeletonization algorithm are as follows: The point with the largest distance from the object's boundary is computed using the Euclidean distance field, which is used as an input for the fast marching propagation. The geodesic distance inside the object starting at the maximum point is computed using fast marching propagation.

If $\boldsymbol{d}$ denotes the distance value of the Euclidean distance field and $\boldsymbol{D}$ represents the maximum value of the field dataset, then the speed is given by

$$speed = \left(\frac{d}{D}\right)^2.$$

Using the speed image, the fast marching algorithm computes the geodesic distance from the start point to each voxel. Then, the furthest point from the global maximum distance point is used as the start point of the branches, and the remaining points of the branch are determined by performing a gradient descent back-tracking procedure satisfying the following equation on the fast marching time-crossing map:

$$\frac{d\boldsymbol{C}}{dt} = -\frac{\nabla T}{|\nabla T|}, \boldsymbol{C}(0) = \boldsymbol{p}_f,$$

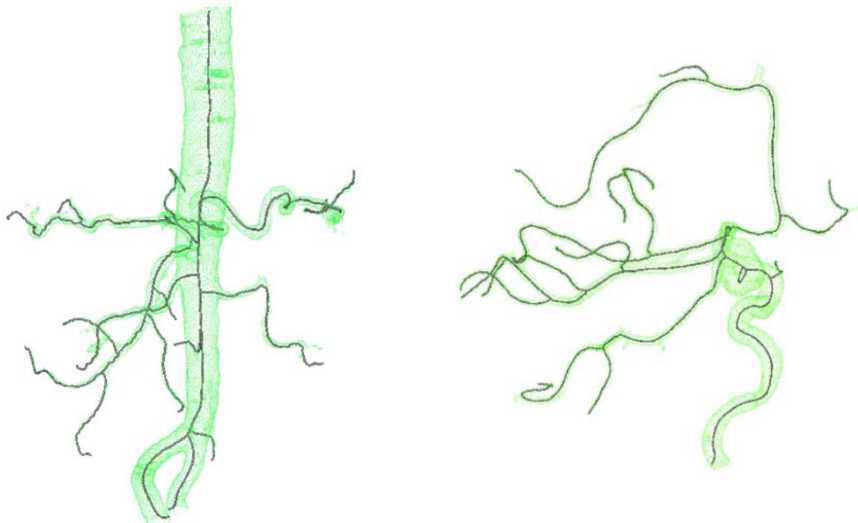

Figure 17 Skeletons extracted by [63] (Left) Descending aorta, renal and mesenteric arteries (Right) Brain blood vessels

where $\boldsymbol{C}(t)$ denotes the centerline and $\boldsymbol{p}_f$ represents the furthest geodesic distance point.

The above process is repeated to determine further branches which form the skeleton of the object. All points in the previously calculated branches are used as start points for the fast marching method. The geodesic distance furthest point from this initial set of start points that is found by the fast marching method will now be the furthest point from the current skeleton and the start point of the new branch. From this start point, another branch of the skeleton can be determined by gradient descent in the time-crossing map. this

challenge, we measured and compared the detection accuracy results.

3.3 Graph Construction

The constructed skeleton is represented as a graph $G = (V, E)$ in Figure 18. Each branch B_i (a white node in Figure 18) becomes a node of G, and then, V is defined as $\rho \cup \{B_1, B_2, \ldots, B_n\}$, where n denotes the number of branches and ρ represents an empty node for the root of G (a black node in Figure 18). E denotes a set of edges, which are contact points between branches.

The skeletonization procedure finds the shortest path from the point with the furthest geodesic distance to the previously constructed branches, and the path becomes a new branch B_i. Therefore, the contact point between B_i and one of the previously constructed branches, B_j, is detected without additional computation. B_i becomes a child node of B_j, and the contact point between B_i and B_j becomes an edge connecting two nodes. Thus, the graph G is constructed simultaneously while extracting skeletons.

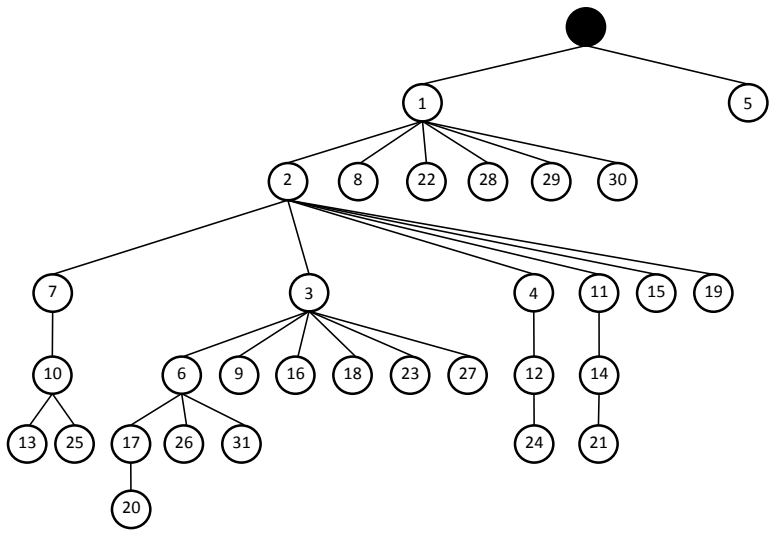

Figure 18 Tree model for 3D vascular structure

3.4 Generation of subtree structures from 3D tree model

After the tree construction, we divide the tree model into several subtrees on the basis of the following rules:

- A subtree is connected.
- $\bigcup_i^m ST_i = G$, where m denotes the number of subtrees and ST_i represents a subtree.

- $ST_i \cap ST_j = \emptyset$ or e_k, where $e_k \in E$.

The trees are divided according to the length of vessels and the connectivity. Hence, a weight for each node is computed on the basis of the length before the subtree separation. The weight of a node is defined as the number of skeleton voxels in the node and its descendants. The weight for a node is initialized as the number of voxels included in the node. Next, the weight is updated by adding the weight of a child node to the weight of its parent node while going up from each leaf node to the root node ρ. Through this process, the weight of a node N is updated as the number of voxels of a subtree whose root node is N, and the weight of the root node ρ becomes the number of all voxels on the skeleton. After updating the weights of all nodes in G, the nodes are sorted in the descending order of the weights.

Algorithm 1 is the pseudocode for a tree update, which inserts a new node corresponding to a new branch with a weight and updates the weights of its ancestor nodes. All points in the previously constructed branches have indexes stored index list L, and the intersection point index idx between a new branch and one of the

previously constructed branches is computed during the construction of a new branch.

Algorithm 1. Pseudocode for a tree update

Given an intersection point index idx and a length l of a new branch, along with the index list L

// find a parent node N_p using idx
$i \leftarrow 0$
while $idx > L[i]$ **do**
    $i \leftarrow i + 1$
end
$N_p \leftarrow Node_i$
$L[L.end + 1] \leftarrow (L[L.end] + l)$

// make a node for a new branch
initialize a new node N
$N.parent \leftarrow N_p$
add N to the list of child nodes of N_p
$N.weight \leftarrow l$

// update weights
$N_{up} \leftarrow N_p$
while N_{up} is not null **do**
    $N_{up}.weight \leftarrow N_{up}.weight + l$
    $N_{up} \leftarrow N_{up}.parent$
end

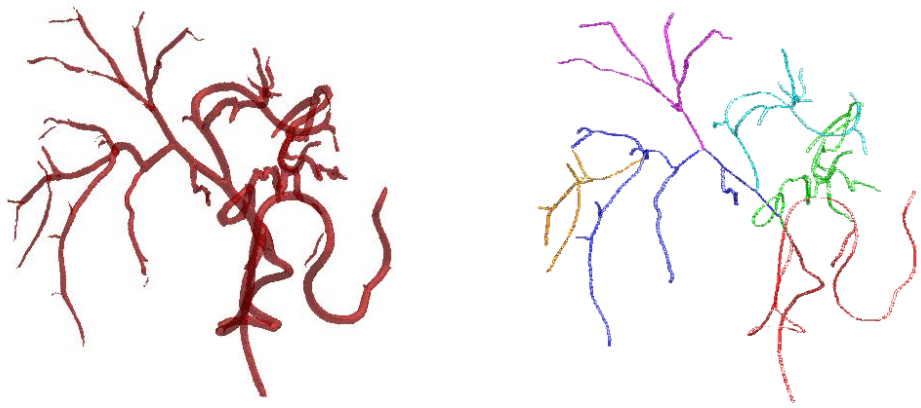

(a) (b)

Figure 19 Separation of a tree. (a) Segmented 3D vessels from CTA. (b) Their skeleton divided into six subtrees.

To divide a tree into subtrees, all nodes of G are initially set as ST_0, and the child nodes of the root node ρ are inserted into a priority queue. Subsequently, the node with the largest weight in the priority queue is selected as the root node of a new subtree. Then, all descendants of the selected node are updated as ST_1, and the child nodes of the selected node are inserted into the priority queue. This process is repeated while the number of subtrees is smaller than a given number, which is set to 6 in our implementation. The parameter study about the number of subtrees is explained in Section 5.5. Algorithm 2 shows the pseudocode for separating a tree G into a

(a) (b) (c)

Figure 20 DSA image and projection of 3D vascular centerlines. (a) DSA image. (b) Projection of the corresponding 3D subtree for the DSA image. (c) Projection of the whole tree.

given number, *max_num*, of subtrees after the tree construction.

Figure 19 shows the 3D vessels and their skeleton, which is separated by the proposed method. In Figure 19 (b), each color represents a subtree. The tree is divided exactly on a junction point, and each subtree is connected. Then, one of the subtrees can have a similar range with the given DSA image since the injection medium is inserted near the junction point and flows into the closely connected vessels. Figure 20 shows that the DSA image and the projection of the subtree can display a similar range.

Algorithm 2. Pseudocode for subtree separation

```
Given the tree G

initialize a priority queue PQ
set the label of every node as 0

label ← 1
push every child node of ρ into PQ

// pop the node with the largest weight among the child nodes of the root node
node ← PQ.pop()

    // repeat while the number of subtrees is smaller than max_num
while label < max_num and PQ is not empty do

    push every child node of node into PQ
    initialize a queue Q
    Q.push(node)

    // update the labels of all descendants
    while Q is not empty do
        n_i ← Q.pop()
        Set the label of n_i as label
        for each child node n_c of n_i
            Q.push(n_c)
        end
    end

    // pop the node with the largest weight
    node ← PQ.pop()
    label ← label + 1
end
```

Chapter 4. Locally Adaptive Registration

To use 3D CTA data as a roadmap during an intervention procedure, an accurate registration between the CTA and the DSA images is necessary. During an intervention, a catheter moves through an artery and contrast medium is injected near the catheter. Then, the injected area is projected to produce new DSA images. Through this process, very limited areas of the vascular structure are displayed in the DSA. Therefore, it is difficult to match the DSA with the entire 3D vessel structure. In this study, we overcome this problem by comparing the DSA with the 3D subtrees constructed as discussed in the previous section, not with the entire structure. By running the registration process with only a part of the structure, we can find the correct transformation parameters for the given DSA image.

The method consists of three steps. First, we extract vessel centerlines from the DSA images (Section 4.1). Subsequently, we find the best matched subtree with vessel centerlines (Section 4.2). Finally, a rigid registration between the 2D centerlines and the selected subtree is conducted (Section 4.3).

4.1 2D centerline extraction

To find the best matched subtree with DSA, the centerlines are extracted from DSA, and the dissimilarity between the centerlines and each subtree is computed. The subtree with the smallest dissimilarity is selected as the matched subtree with the current DSA.

We consider two cases of input image. First, we use a single DSA image which is manually selected from DSA sequence. The chosen image should have dominant features suitable for 2D−3D registration. Next, we assume that input images are given from actual intervention. Then, we obtain image sequence which consists of several angiographic image frames. Moreover, the image quality of angiographic sequence are usually very low because of low dose radiation. Prolonged exposure to X−ray radiation adversely affects the human body, and therefore, physicians prefer to obtain X−ray images with the lowest possible radiation dose. Hence, we consider very low dose X−ray angiographic image sequence as an input for 2D−3D registration.

In Section 4.1.1, we explain the centerline extraction from one 2D DSA image, and then, in Section 4.1.2, we extend the centerline

extraction algorithm in order to apply to low dose angiographic image sequence.

4.1.1 Extraction from a single DSA image

The centerlines of the 2D DSA are extracted in a way similar to that used for the 3D skeleton. The 2D vesselness measure [57] is calculated for each pixel, and we binarize the image data with a threshold for the vesselness measure. Then, we perform a 2D connected component analysis and detect the largest connected component as a 2D vessel. The threshold for the 2D vesselness measure is set to 0.7. Further, the centerline is extracted by the augmented fast marching method [65]. Figure 21 shows a process of the centerline extraction process. The images in Figure 21 are inverted for clear visibility. The centerlines extracted by the above process (Figure 21 (d)) are used as features for 2D−3D registration in next section.

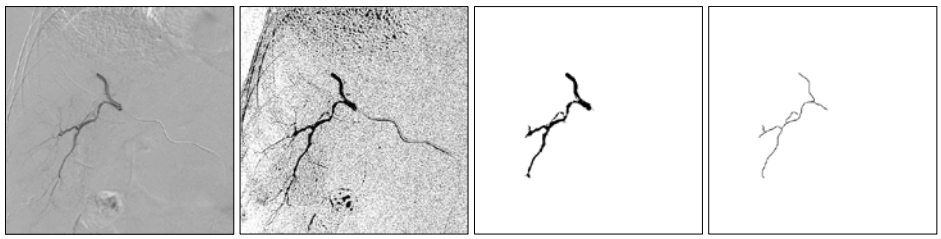

(a) (b) (c) (d)

Figure 21 2D centerline extraction process. (a) Input DSA image. (b) Vesselness measure. (c) Vessel segmentation. (d) Centerline extraction.

4.1.2 Extraction from angiographic image sequence

During intervention, a 2D angiographic image sequence is obtained, and 2D features are extracted from the sequence for a 2D−3D registration. First, we enhance the image quality by temporal filtering. Next, a DSA image is obtained by subtracting a mask image obtained before contrast medium injection from each frame, followed by binarization with a threshold for the vesselness measure. After performing a connected component analysis, we remove the components, which are small and far from the center of the image. Next, all the images are merged into a single image by an OR operation and we designate the largest connected component in the merged image as being 2D vessels. Lastly, the centerlines, which are

used as features for the 2D−3D registration, are extracted by implementing the fast marching method [65].

The temporal filtering is defined to be the first−order recursive equation proposed by Aach et al. [80].

$$x(t) = x(t-1) + K(t) \cdot [y(t) - x(t-1)] \quad (1)$$

Here, $y(t)$ is the original noisy signal of a pixel at time t and $x(t)$ is the filtered signal. This equation is applied to every pixel. The filter gain $K(t)$ is updated using the following rule.

$$K(t) = K(t-1)/[K(t-1) + \alpha(t)] \quad (2)$$

Here, $\alpha(t)$ represents the continuity probabilities defined as a monotonically decreasing function of $|y(t) - x(t-1)|/s(t)$. To compensate for the motion between frames, we use the motion compensated signal $y'(t)$ obtained by using a block−matching algorithm [81] in the place of $y(t)$ in Eq. (1) and (2).

Figure 22 shows the process of 2D feature extraction from the image sequence. Through the process, we obtain one image with 2D vessel centerlines such as Figure 22 (f), which are used for 2D−3D registration in next section.

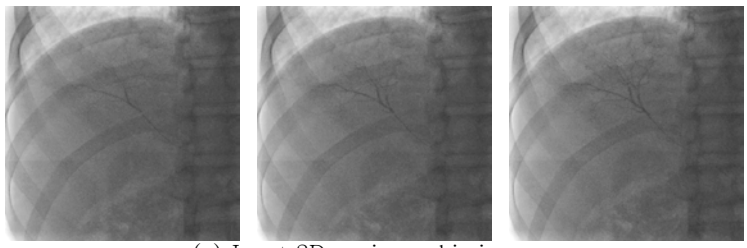

(a) Input 2D angiographic images

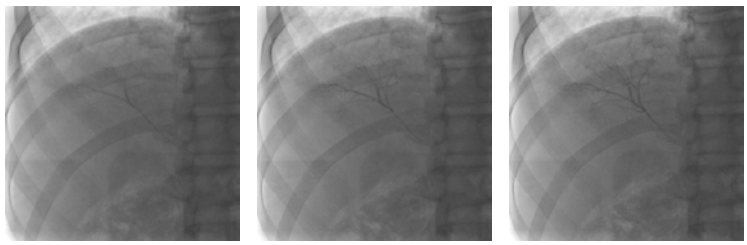

(b) Temporal filtered images

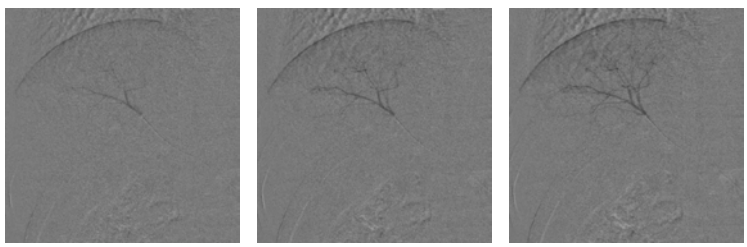

(c) DSA images

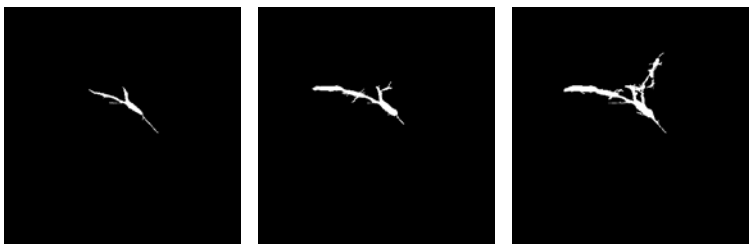

(d) Vessel segmentation on each frame

(e) Merged vessels

(f) Centerline extraction

Figure 22 2D centerline extraction from angiographic image sequence

4.2 Coarse registration for the detection of the best matched subtree

To find the best matched subtree with DSA, the centerlines are extracted from DSA, and the dissimilarity between the centerlines and each subtree is computed. The subtree with the smallest dissimilarity is selected as the matched subtree with the current DSA.

The dissimilarity is defined as the difference between a projected subtree and the 2D centerlines. To be accurate, the dissimilarity of ST_k is the mean of the distance differences between points on the projected subtree and the corresponding points on the 2D centerlines.

In Section 3, ST_k is defined as a set of branches labeled k, and each branch consists of voxels on a part of the 3D skeleton. Hence, ST_k can be re-defined as a set of voxels on the skeleton with the label k. Thus, we can define the dissimilarity of ST_k as follows:

$$f(k) = \frac{1}{n_k} \sum_{x_i \in ST_k} \|\Phi(\mathrm{T}x_i) - y_i\|, \quad (3)$$

where n_k denotes the size of ST_k, Φ represents a projection function, T indicates a 4×4 transformation matrix, and y_i denotes the closest point on the 2D centerlines to $\Phi(\mathrm{T}x_i)$. The dissimilarity

is used as the cost function for a coarse registration between the 2D centerlines and a subtree. By the coarse registration, the dissimilarity of each subtree is minimized, and then, the subtree with the smallest dissimilarity is selected as the best matched subtree.

The registration in the selection step is only concerned with the translation transformations for the fast computation, and a rigid registration is conducted in the subsequent step. Therefore, when a parameter set for ST_k to be optimized is given as $P_{\mathrm{T},k} = [t_x, t_y, t_z] \in \mathbb{R}^3$, T in Eq. (3) is defined as $\mathrm{T} = \begin{bmatrix} 1 & 0 & 0 & t_x \\ 0 & 1 & 0 & t_y \\ 0 & 0 & 1 & t_z \\ 0 & 0 & 0 & 1 \end{bmatrix}$.

The function $\Phi : \mathbb{R}^3 \rightarrow \mathbb{R}^2$ projects a 3D point onto a detector plane and is determined by using the information in the DICOM header [48]. Then, we draw a ray from a source to each voxel $x_i \in ST_k$ and directly compute a location to be projected on the 2D plane [82]. It is considerably more efficient to project the skeleton directly than to use a ray-casting algorithm [83] because the skeleton is only a small portion of the entire 3D volume.

We need to find the closest point of the 2D centerlines for each projected point in order to calculate Eq. (3) whenever the transformation of a subtree is changed. This can be considerably

faster by using a distance transform [84]. We compute a distance transform for the 2D centerlines by using the algorithm in [85], and the computation is requested only once because the 2D centerline is reference data and therefore, not changed. The distance transform for the 2D centerlines is denoted as $\mathbf{DT_{cls}}$. Then, Eq. (3) is defined as follows:

$$f(k) = \frac{1}{n_k} \sum_{x_i \in ST_k} \mathrm{DT_{cls}}\big(\Phi(\mathrm{T}x_i)\big) \tag{4}$$

For each subtree, we optimize $P_{\mathrm{T},k}$ by using the cost function, Eq. (4). The parameters are initialized to zero. We use the Nelder–Mead optimizer as the optimization algorithm, which shows a good performance for the 2D–3D registration among the local optimization algorithms [61]. The final value of the cost function through the optimization becomes the dissimilarity for each subtree, and then, the subtree with the smallest dissimilarity is chosen as the best matched subtree to the DSA data. The parameter for the selected subtree ST_k, $P'_{\mathrm{T}.k} = [t'_x, t'_y, t'_z]$ is used as the initial parameter value in the next step.

4.3 Fine registration with selected 3D subtree

In Section 4.2, we concerned ourselves only with the translation transformation for the fast computation, and in order to obtain more correct results, we now conduct a rigid registration for the selected subtree. Eq. (4) is used as the cost function, but the transformation matrix T in Eq. (4) is re-defined as $\mathrm{T} = \mathrm{T_T} \cdot \mathrm{T_R}$, where $\mathrm{T_T}$ denotes a translation matrix and $\mathrm{T_R}$ represents a rotation matrix. Given a parameter set $P = [t_x, t_y, t_z, r_x, r_y, r_z] \in \mathbb{R}^6$, the matrices are defined as follows:

$$\mathrm{T_T} = \begin{bmatrix} 1 & 0 & 0 & t_x \\ 0 & 1 & 0 & t_y \\ 0 & 0 & 1 & t_z \\ 0 & 0 & 0 & 1 \end{bmatrix} \text{ and}$$

$$\mathrm{T_R} = \begin{bmatrix} \cos(r_z) & \sin(r_z) & 0 & 0 \\ -\sin(r_z) & \cos(r_z) & 0 & 0 \\ 0 & 0 & 1 & 0 \\ 0 & 0 & 0 & 1 \end{bmatrix} \begin{bmatrix} \cos(r_y) & 0 & -\sin(r_y) & 0 \\ 0 & 1 & 0 & 0 \\ \sin(r_y) & 0 & \cos(r_y) & 0 \\ 0 & 0 & 0 & 1 \end{bmatrix} \begin{bmatrix} 1 & 0 & 0 & 0 \\ 0 & \cos(r_x) & \sin(r_x) & 0 \\ 0 & -\sin(r_x) & \cos(r_x) & 0 \\ 0 & 0 & 0 & 1 \end{bmatrix}$$

The initial value of P is set as $[t'_x, t'_y, t'_z, 0, 0, 0]$ when $P'_{\mathrm{T}.k} = [t'_x, t'_y, t'_z]$ is obtained in the previous section and the Nelder–Mead optimizer is used.

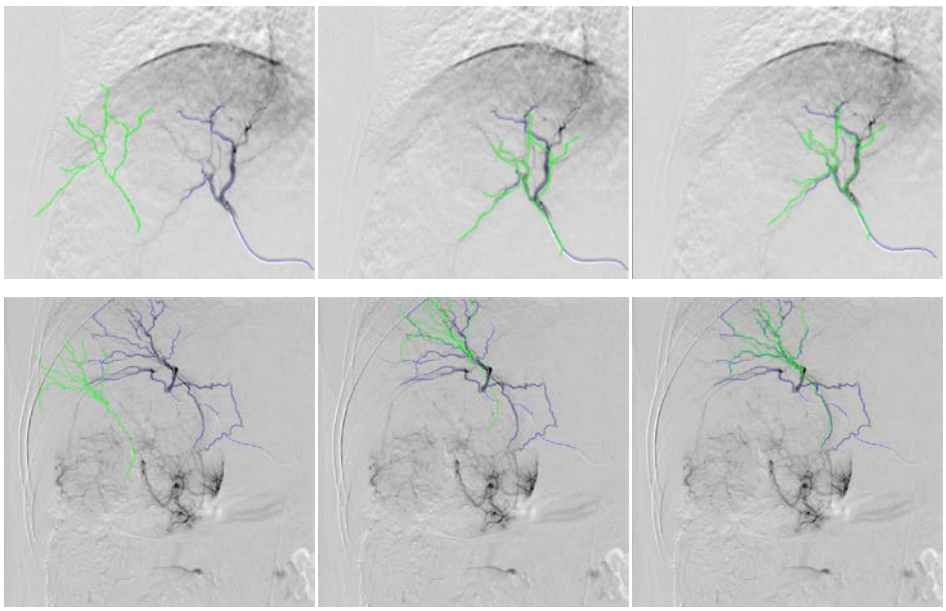

Figure 23 Results of the proposed algorithm. The blue line denotes the centerline of the 2D vessels in the DSA, and the green line represents the projection of the corresponding subtree to the DSA. From left to right, the projection is computed after the initial alignment, the subtree selection, and the fine registration.

Figure 23 shows how the proposed registration algorithm works. The green lines represent the projected subtree, which is selected as the best match by the proposed method. The first image is a projection after the initial placement, the second after the selection step, and the third after the rigid registration.

Chapter 5. Experimental Results

5.1 Materials

Ten breath-hold DSA datasets were tested to verify that the proposed algorithm found the appropriate subtree and computed the correct transformation parameters. Each DSA dataset had the corresponding CTA scans, and we used four CTA scans obtained from different patients (Table I). All datasets were obtained using a C-arm CT scanner of Siemens. The number of slices per CTA scan ranged from 343 to 441, and each slice had a size of 512 × 512. The pixel spacing and the slice interval were all 0.4 mm. DSA datasets had a pixel spacing of 0.216 to 0.308 mm and primary and secondary angles of 0° to 30°. The resolution of all DSA datasets was 1024 × 1024. The proposed method was implemented in MATLAB and tested on an Intel i7 desktop system with a 3.40-GHz processor and 8-GB memory.

Table I. CTA and DSA datasets

CTA	1	2	3	4
Number of DSA datasets	1	2	2	5
Dataset number	1	2–3	4–5	6–10

In addition, to verify the proposed algorithm for low-dose image sequence, we tested four breath-hold low dose angiographic image sequences. We used the same CTA scan explained in the above paragraph, and for each CTA scan, one corresponding image sequence was tested. Each sequence contained 50-80 frames and the resolution of each frame was 512×512. Low-dose images were acquired using 2% of the X-ray radiation dose that is used for acquiring high-dose images. The scan parameters for each dataset are summarized in the following table.

Table II. The scanning parameters of the datasets

Datasets	1	2	3	4
X-ray tube current (mA)	65	65	65	65
Image area dose product (Gym^2)	5.1	3.69	2.23	1.86
Pixel spacing (mm)	0.433	0.578	0.433	0.578

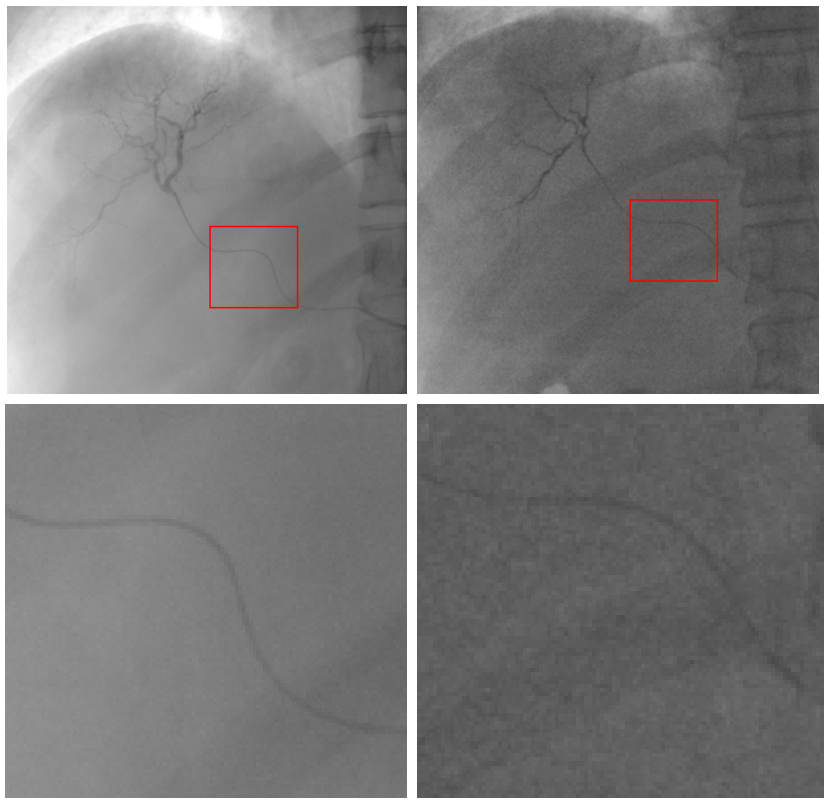

Figure 24 Comparison of the image quality between a high-dose image (left column) and a low-dose image (right column)

5.2 Phantom study

We validate the correctness of the algorithm with the simulated DSA images. The images are obtained by projecting CTA scans with changing transformation parameters. To generate a simulated DSA image, we project CTA scans onto a 2D plane twice by using the DRR

computation in [83]. First, we project the data without preprocessing and then, obtain the simulated X-ray image with all vessels of the CTA data projected (Figure 25 (a)). Next, we set the value of vessels that we want to display on the DSA as zero. To find the region to be simulated, we choose the seed randomly on the subtree to be projected and run the region growing algorithm from the seed. Since we assign the minimum value on the intersection point between subtrees, the region growing does not flow into other subtrees. After changing the value of CTA data, we project it with the same parameter as in the first projection (Figure 25 (b)). Lastly, we subtract the second projection image from the first projection image. Thus, we obtain the simulated DSA image with vessels contrasted only in a limited scope. Figure 25 (c) shows the DSA image obtained by using the above procedure. Following the procedure, six simulated datasets are obtained. We construct two pairs of simulated X-rays and CT images, and for each pair, we obtain three datasets by changing the translational and rotational parameters.

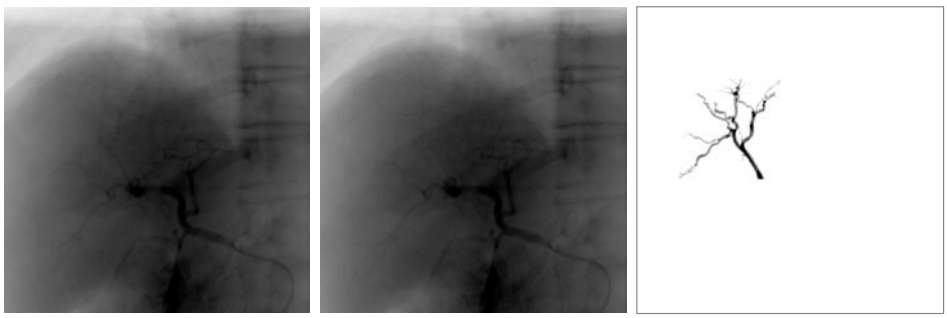

(a) (b) (c)

Figure 25 Simulated DSA construction. (a) DRR without vessel selection. (b) DRR after vessel selection. (c) Simulated DSA.

The proposed method finds the appropriate subtree and computes the transformation parameters for a simulated DSA image. Then, the result image is obtained by projecting the selected subtree according to the transformation parameters. To measure the accuracy of the results, we define the junction points of the vascular centerlines as the anatomical feature points. For each simulated DSA image, 5–10 junction points are selected manually as the feature points. We limit the number of feature points to less than 10 because the DSA image shows only a small part of the vasculature, and it is difficult to find more than 10 feature points in one image. Subsequently, in the registered result image, the corresponding points to the feature points of the DSA image are found, and then, the

error measure of the validation of the proposed algorithm can be defined by the distance between the feature points and the corresponding points as follows:

$$E_{feat} = \frac{1}{n} \sum_{r_i \in \Omega} \| r_i - p_i \|, \quad (5)$$

where Ω denotes the set of the feature points in the reference image, n represents the number of feature points, and p_i indicates the corresponding points of r_i in the 2D projection image. Table III shows E_{feat} for each simulated DSA image.

In another method of the validation of the proposed method, since the simulated DSA is constructed with the predefined transformation parameters, we can verify the capture range of the proposed method. The capture range is defined as the portion of parameter space within which the registration algorithm can be expected to converge to the correct solution [16]. We execute the proposed algorithm from a

Table III. Accuracy assessment results of simulated DSA images

Dataset	1	2	3	4	5	6
E_{feat} (mm)	1.492	0.505	1.7462	0.452	0.631	0.760

Table IV. Capture range of simulated DSA images

Dataset	Pair 1 (1-3)	Pair 2 (4-6)
Translational parameters (mm)	57.3	69.3
Rotational parameters (degree)	30.7	32.3

large number of starting positions with respect to the predefined transformation parameters and determine the registration converged to the correct solution when the error E_{feat} is smaller than 3 mm. The capture range for each dataset is determined as the largest successful translational and rotational parameters through approximately 100 registrations. Table IV shows the average of the capture range for each pair.

5.3 Performance evaluation

5.3.1 Evaluation for a single DSA image

We tested the proposed method for 10 clinical datasets. We

evaluated the correctness of the proposed method by dividing it into two steps: subtree selection and fine registration.

In the subtree selection step, the dissimilarity of each subtree is computed and the subtree with the smallest one is chosen as the appropriate subtree for the DSA image. Table V shows the dissimilarity of all subtrees for each dataset, and the selected subtree is written in bold type.

In the case of dataset 2, subtree 5 is selected because the dissimilarity of subtree 5 is the smallest among the six subtrees. Figure 26 shows the DSA and all subtrees for dataset 2, and we can confirm that the subtree selected in the selection step of the proposed method correctly corresponds to the DSA.

Table V. Dissimilarity comparison between subtrees

Dataset number	Subtree					
	1	2	3	4	5	6
1	95.743	66.224	16.146	**14.556**	18.161	22.520
2	89.814	63.392	44.013	16.897	**6.09**	28.897
3	54.643	14.659	17.327	22.313	27.776	**3.592**
4	27.668	13.584	16.886	11.685	**9.830**	14.749
5	49.689	34.196	67.671	37.672	**8.891**	43.214
6	43.276	37.096	**20.502**	31.874	57.096	42.504
7	46.516	31.155	115.553	23.681	30.638	**9.905**
8	41.169	30.027	81.615	11.688	28.380	**10.002**
9	54.921	**25.154**	67.687	30.278	44.366	32.262
10	49.857	63.092	86.706	17.040	35.869	**7.115**

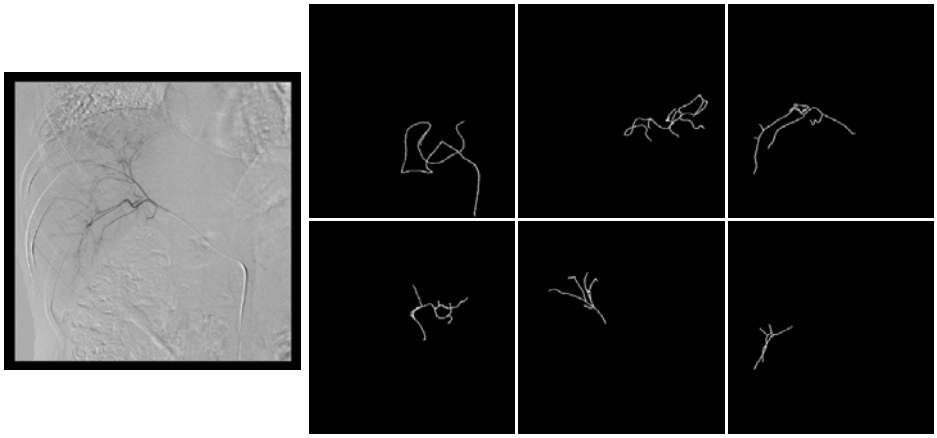

Figure 26 DSA and subtrees of the 3D vascular structure. The subtrees are labeled 1, 2, 3, 4, 5, and 6 from left to right, and top to bottom. The selected subtree is displayed in the red box.

Figure 27 describes the convergence of the subtrees for dataset 2. Each subtree converges through the optimization process. The dissimilarity of subtree 5 starts from 84.76 and finally stops at 6.09, which is the smallest value among the six subtrees. Hence, subtree 5 is selected as the best matched subtree.

Next, we verify the accuracy of the fine registration step by considering the distance errors between the centerline of the DSA and the projected centerline of the registered subtree. The distance error is measured in the same way as in the phantom study. The junction points on the centerlines of the DSA image are defined as the anatomical feature points, and Eq. (5) is applied. Table VI summarizes the distance errors of the 10 datasets. For all the datasets, the errors before the registration process range from

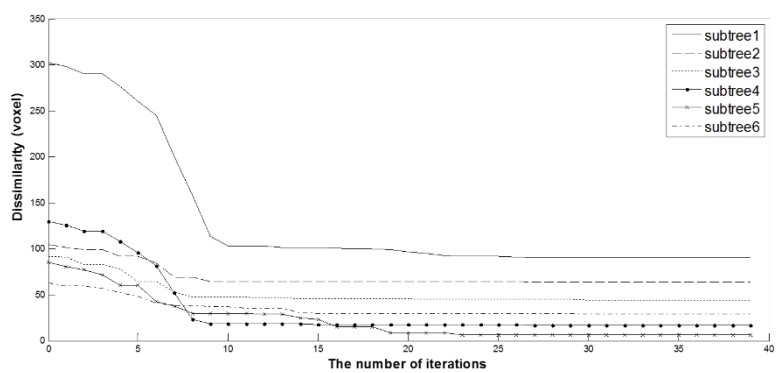

Figure 27 Convergence graph of each subtree for dataset 2

16.688 to 55.770 mm, and the average value is 40.114 ± 12.694 mm. After the registration process, the average value of the errors becomes 2.337 ± 1.940 mm, ranging from 0.087 to 6.169 mm. Further, Figure 28 shows the DSA overlaid with vascular tree structures. Figure 28 (c) shows that the entire vascular tree was accurately overlaid on the DSA after fine registration by using only the subtree structures shown in Figure 28 (b). In contrast, Figure 28 (f) shows the overlaid image with a relatively large difference between the DSA and the whole tree. The 2D centerlines are too short to find a correct transformation, and this leads to errors in the registration process.

Table VI. Accuracy assessment results of registration for a single image

Dataset	Initial error (mm)	Error after fine registration (mm)
1	55.770±0.532	1.654±0.928
2	29.547±1.080	1.778±0.808
3	32.741±2.331	5.571±3.215
4	16.688±0.177	0.087±0.173
5	43.083±0.548	1.157±1.230
6	51.141±2.668	1.342±0.742
7	41.243±1.456	1.757±1.096
8	55.634±1.959	2.361±1.648
9	55.431±2.274	3.830±2.711
10	29.649±1.945	6.169±4.198

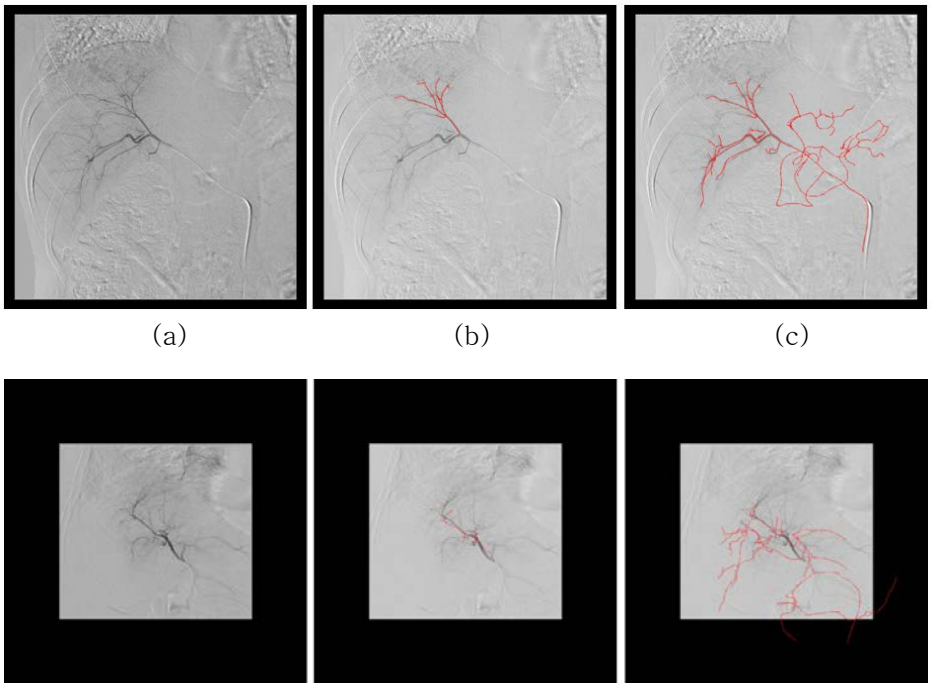

Figure 28 DSA image overlaid with vascular tree structures. (a), (d) Original DSA image. (b), (e) DSA image overlaid with the selected subtree after fine registration. (c), (f) DSA image overlaid with the entire vascular tree after fine registration.

Figure 29 shows the convergence graph for datasets 2 and 8, including the selection step and the fine registration step. For dataset 8, the final dissimilarity in the selection step is 10.002. Subsequently, in the fine registration step, the optimization process starts with the addition of the translation parameters computed in the selection step to the rotation parameters. Then, the final dissimilarity reaches 3.419

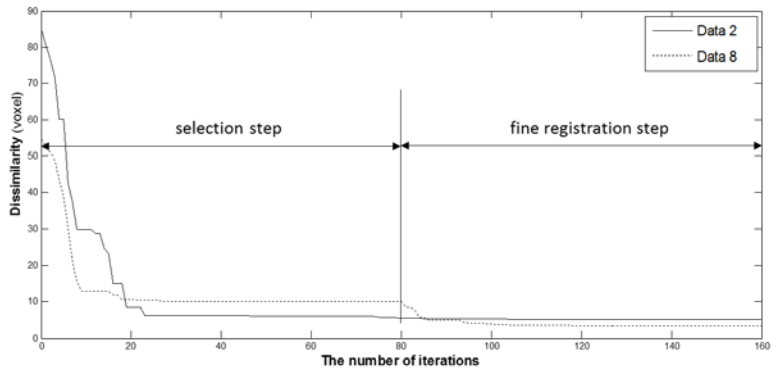

Figure 29 Convergence graph for datasets 2 and 8

through fine registration.

For the evaluation of the computational performance of the proposed method, we measured the total processing time. The total processing time, averaged over multiple tests for all the datasets, was 95.3 ± 15.6 s. It took 76.0 ± 12.4 s for the subtree selection and 19.3 ± 4.4 s for the fine registration.

5.3.2 Evaluation for angiographic image sequence

We tested the proposed method for four low-dose angiographic image sequences. Figure 30 shows the results for dataset 3. After

2D−3D registration, the 3D vascular structure are registered with vessels on a 2D angiographic image. The error measure is defined as the distance between the feature points and the corresponding points, E_{feat}. Table VII summarizes the distance errors of the 4 datasets. For all the datasets, the errors before the registration process range from 28.994 to 53.270 mm, and the average value is 41.608 ± 8.678 mm. After the registration process, the average value of the errors becomes 3.168 ± 1.211 mm, ranging from 2.358 to 4.566 mm. Although the image quality of the input 2D image sequence in comparison with a DSA image used in previous section, the proposed method still produces highly accurate registration results.

Table VII. Accuracy assessment results of registration for image sequence

Dataset	Initial error (mm)	Error after fine registration (mm)
1	28.994±0.706	2.358±2.198
2	40.401±1.417	4.566±2.026
3	43.766±0.499	1.631±2.032
4	53.270±1.682	4.115±3.944

Figure 30 The result of the proposed algorithm for image sequence. The red line represents the projection of the corresponding subtree into the input angiographic sequence. The leftmost image is the projection of the selected subtree before the registration and (b) shows the projection after the registration. (c) is the projection of the whole 3D tree after the registration process

5.4 Comparison with other methods

We compared the accuracy of the proposed method with two 2D-3D registration methods. The first is the registration algorithm based on the distance transform using an entire tree [5], and the second is the state-of-the-art registration algorithm for liver catheterization [24]. Ruijters defines the cost function as the multiplication of the

vesselness measure and the distance transform. Since Ruijters' method [5] uses the whole skeletons of the 3D vessels in the optimization process, it is difficult to find the exact transformation for the current input DSA image, which has a very small part of the vessel structures. In contrast, the proposed method and Ambrosini's method [24] find the best matched part from the entire structure and then, compute the transformation parameters with the partial structure. They remove irrelevant vessels from the projection image of the 3D vessels, and thus, the corresponding points between the 2D and the 3D vessels are defined correctly, which enables the optimization process to find the correct solution.

However, Ambrosini's method [24] finds the best matched leaf vessel centerline in a 3D tree corresponding to the catheter in the 2D fluoroscopic image. When the catheter does not have a predominant feature or is too short, the method fails to find the correct leaf centerline. Moreover, since the cost function for the registration uses only the catheter and its corresponding leaf vessel centerline, the accuracy of matching vessels is relatively lower than that of the proposed method.

Table VIII shows the distance errors obtained using Eq. (5) of the proposed method, Ruijters' method, and Ambrosini's method for the same datasets. The average error in the case of Ruijters' method is 53.290 ± 37.378 mm, which indicates that it is difficult to find the correct solution with a whole 3D tree in liver catheterization. The proposed method and Ambrosini's method [24] show considerably lower average errors, 2.337 ± 1.940 mm and 12.505 ± 12.441 mm, respectively. However, Ambrosini's method [24] failed to find the appropriate centerline for dataset 5 because the catheter is too short;

Table VIII. Accuracy comparison of registration

Dataset	Proposed method (mm)	Ruijters *et al.* [5] (mm)	Ambrosini *et al.* [24] (mm)
1	1.654±0.928	75.872±0.522	9.259±1.510
2	1.778±0.808	20.015±2.037	4.299±0.957
3	5.571±3.215	23.159±3.769	11.585±3.247
4	0.087±0.173	4.810±1.167	9.238±1.089
5	1.157±1.230	135.320±3.853	48.692±0.801
6	1.342±0.742	70.486±13.108	7.714±3.553
7	1.757±1.096	12.156±8.408	10.013±3.305
8	2.361±1.648	62.501±1.993	6.864±2.935
9	3.830±2.711	59.180±7.561	14.122±3.210
10	6.169±4.198	69.397±21.469	3.265±0.663

this causes a large error. Further, for datasets other than dataset 10, the proposed method shows lower errors than Ambrosini's method. The proposed algorithm had errors of less than 7 mm for all datasets. This comparison demonstrated that the proposed method is successfully devised to find a suitable part for a given DSA image and to accurately register 3D vessels to the DSA image.

Figure 31, Figure 32 and Figure 33 show the results from the proposed method and Ambrosini's method. The left column displays the results by the proposed method and right column shows the results by Ambrosini's method. In the first row, 2D features used for the registration methods are displayed as blue line. The proposed method uses the 2D vessel centerlines extracted from DSA image and Ambrosini et al. use the catheter centerlines extracted from 2D angiographic image. The second row shows which partial vascular structures from 3D vessels are selected for the proposed method and Ambrosini's method, respectively. The proposed method finds the best matched subtree with extracted 2D vessel centerlines. On the contrary, Ambrosini et al. selects the best matched leaf vessel centerline by computing the shape similarity between leaf vessel

centerline and the extracted 2D catheter centerline. Last rows show the final results of two methods. The entire tree is transformed by the registration result, and overlaid onto DSA image and angiographic image, respectively.

As shown in Table VIII, the proposed method shows lower errors than Ambrosini' s method except for dataset 10. Figure 31 shows the results for dataset 4 for which both the proposed method and Ambrosini' s method have successful registration results. On the whole tree, 3D vessels and 2D vessels are correctly registered although there are slightly unmatched vessels which are decided on the features used for selecting the suitable partial structure. Dataset 5 used the same CTA scan with dataset 4, but 2D images are obtained at different view, which induces very different results. Figure 32 shows the results for dataset 5. In this dataset, the proposed method succeeds in selecting an appropriate subtree and obtains a good registration results. On the contrary, Ambrosini's method fails to find a suitable leaf vessel centerline because the shape of the catheter is a straight line. It makes difficult to select a correct vessel centerline from 3D structure. Therefore, the registration error of Ambrosini's method becomes very large, 48.692, while the registration of the

proposed error is only 1.157.

Figure 33 represents the results for dataset 10 which has lower registration error in Ambrosini's method. Both methods succeed to find a suitable partial structures from whole 3D structure. However, the proposed method computes the transformation with the subtree located at the upper area of 3D structure, which induces relatively large errors in lower area. On the other hand, Ambrosini's method computes the transformation with the vessel centerline located at the center of 3D structure. It makes smaller errors in final registration results.

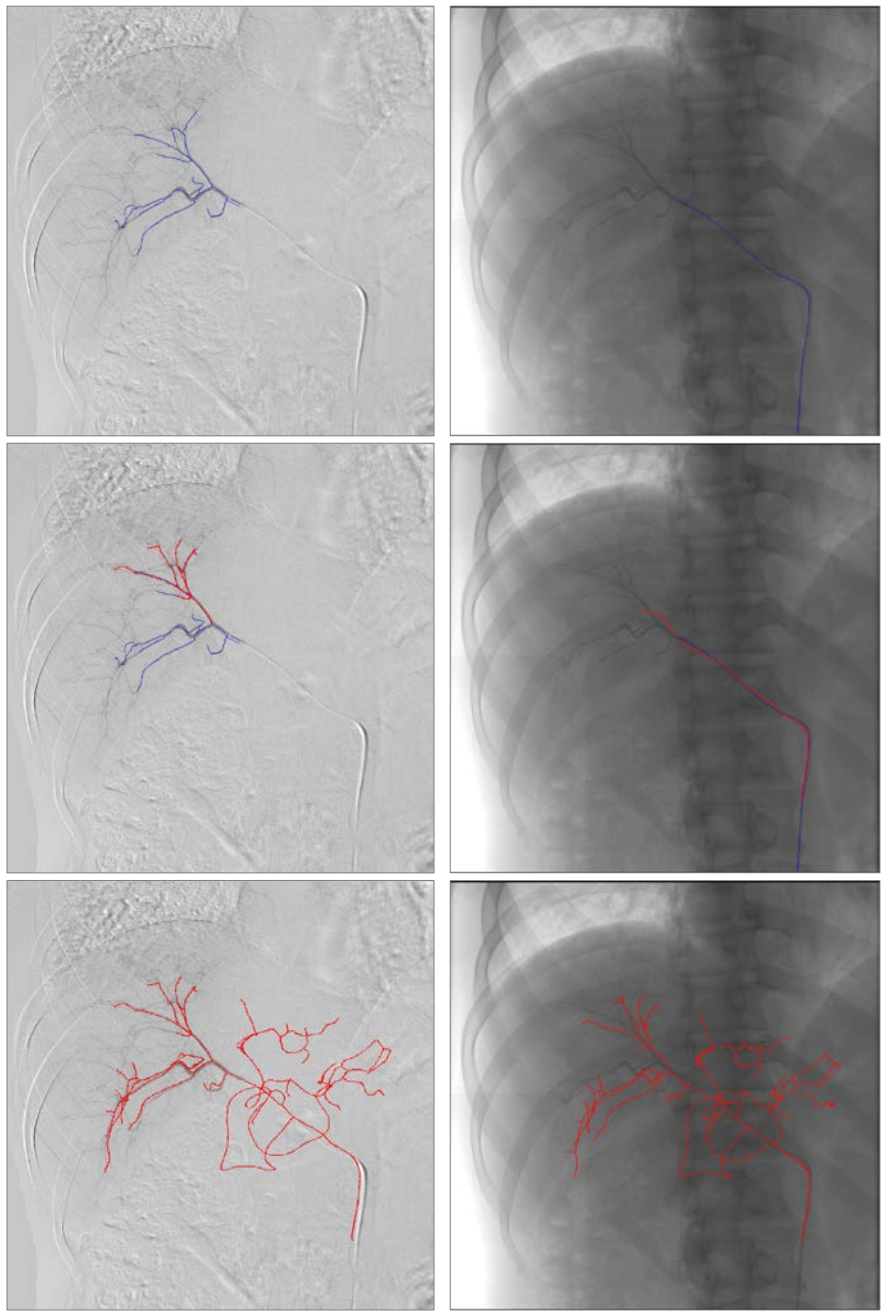

Figure 31 Comparison with Ambrosini's method for dataset 4. Left column is the result of the proposed method and right column is the result of Ambrosini's method.

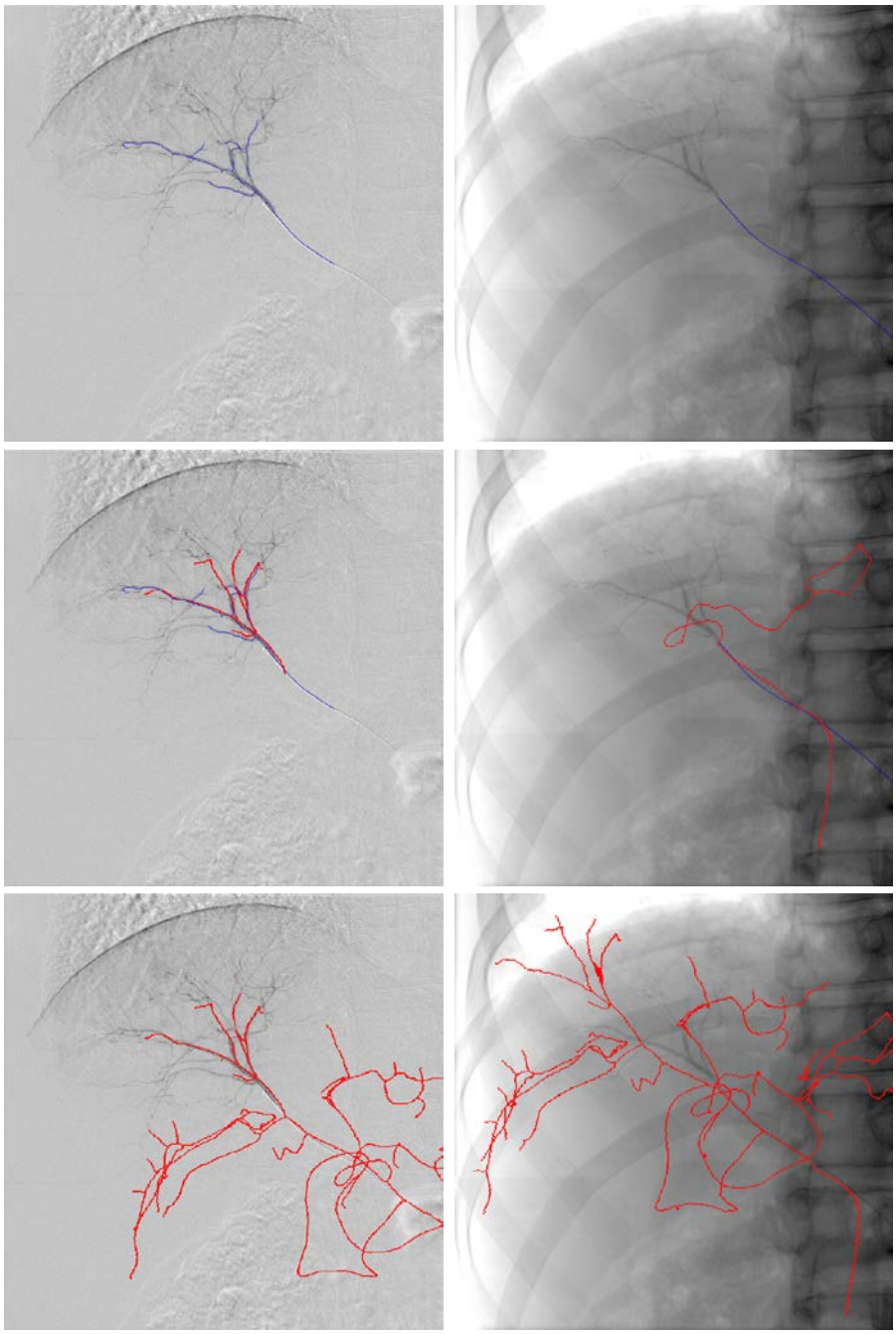

Figure 32 Comparison with Ambrosini's method for dataset 5. Left column is the result of the proposed method and right column is the result of Ambrosini's method.

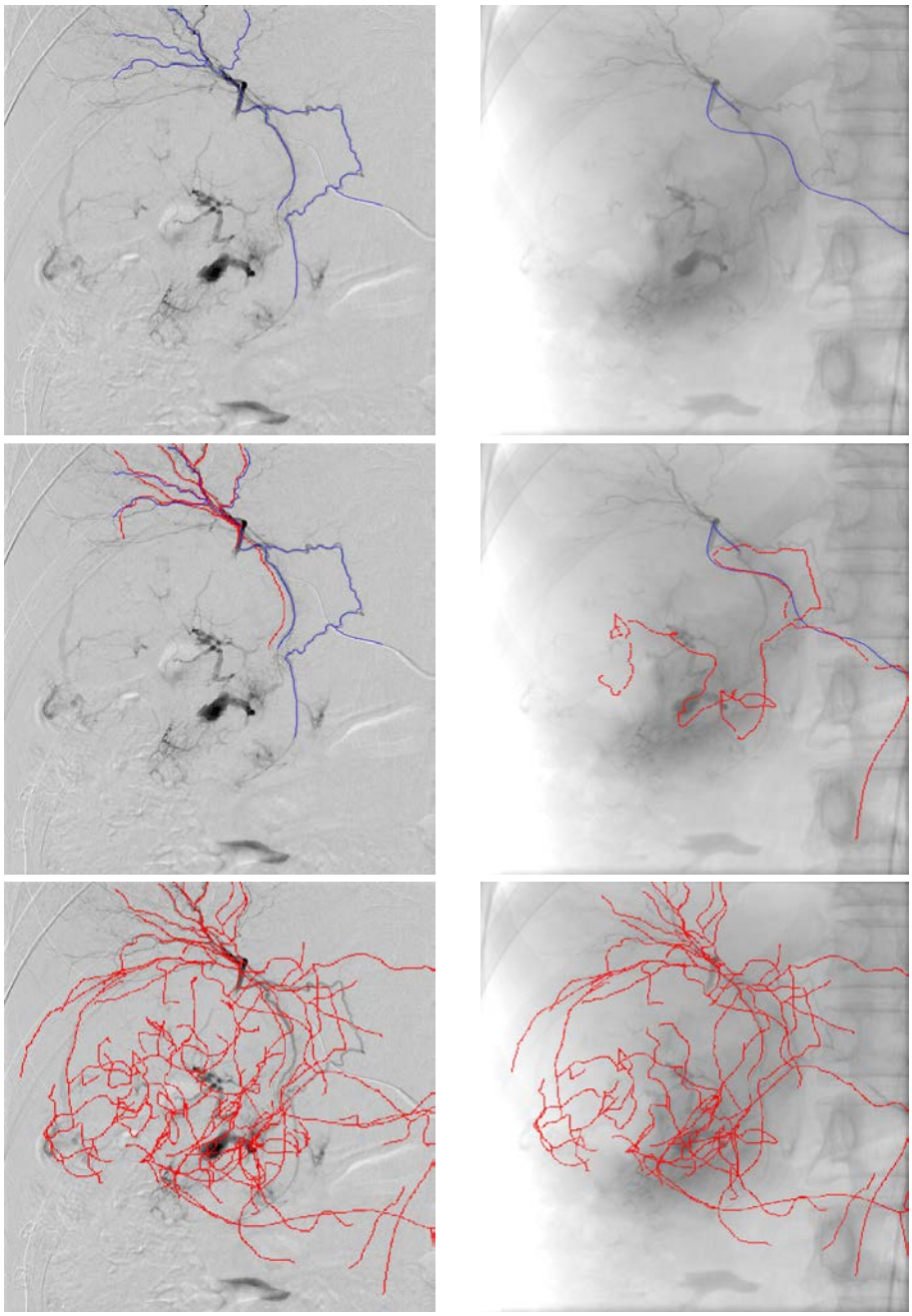

Figure 33 Comparison with Ambrosini's method for dataset 4. Left column is the result of the proposed method and right column is the result of Ambrosini's method.

In addition, we verified that the comparison between registration errors are statistically significant using the Kruskal–Wallis test. The Kruskal–Wallis test is used to evaluate differences among three or more treatment conditions using ordinal data from an independent measures design. The test is an alternative to the single–factor analysis of variance (ANOVA). However, the ANOVA requires numerical scores that can be used to calculate means and variances. The Kruskal–Wallis test, on the other hand, simply requires that you are able to rank–order the individuals for the variable being measured [86].

We run the Kruskal–Wallis test for the accuracy results from three registration methods in Table VIII. The box plot, Figure 34, visualize the summary statistics for each method. Each registration method has different error range and the ranges hardly overlap one another. The numerical analysis shows more specifically that three registration methods have statistically significant differences. With $df = 2$, the chi–square table lists a critical value of 5.99 for $\alpha = 0.05$. The chi–square value obtained from the Kruskal–Wallis test for registration methods is 20.77, and it is much greater that the critical value. In addition, the p–value of the test is 0.00003, which is very

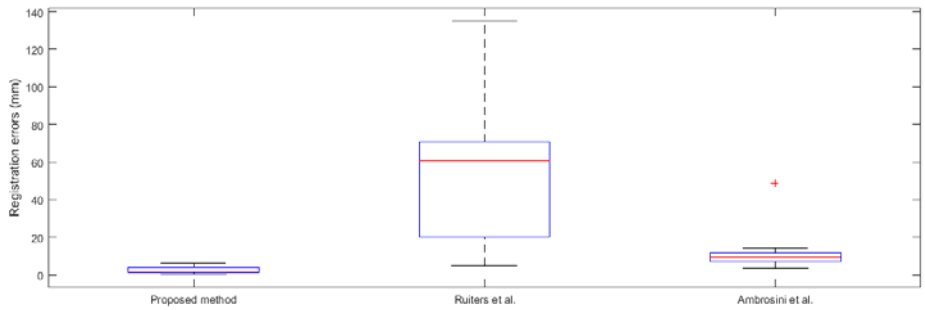

Figure 34 Box plot of registration errors for the proposed method, Ruijters' and Ambrosini's method

low. Therefore, we can conclude that there are statistically significant differences among three registration methods.

5.5 Parameter study

The performance of the proposed method is decided by the number of subtrees. It is possible to select a suitable subtree for a given DSA image only when the subtrees are constructed with an appropriate range. The tree should be divided into subtrees that are sufficiently small to be a subset of the centerlines of the DSA or to have a similar range. In contrast, the computational time for the selection step is

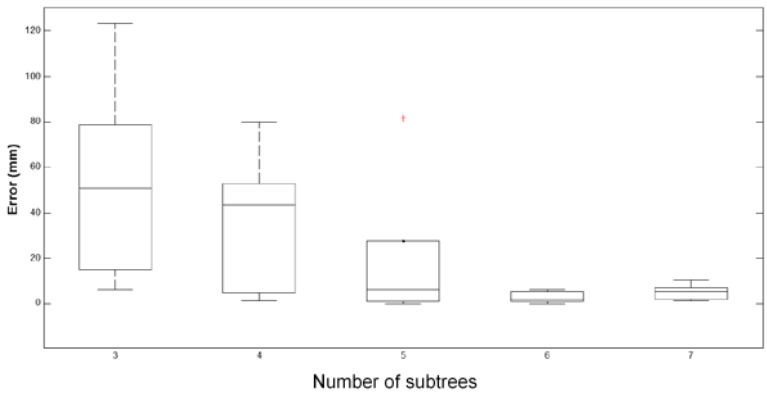

Figure 35 Errors according to the number of subtrees

increased as the number of subtrees increases although the computational time for each subtree is decreased. To decide the optimal number of subtrees, we tested five datasets by changing the number of subtrees from 3 to 7 and evaluating the results of the proposed registration methods by using Eq. (5).

First, we checked the success rate, which is the percentage of the dataset matched with the correct subtree in the selection step. The success rates were 60, 20, 60, 100, and 100(%) for three, four, five, six, and seven subtrees, respectively. In the cases of six and seven subtrees, the correct subtrees were found for all datasets in the selection step. This leads to the high accuracy of the results after the registration process. Figure 35 shows the accuracy of the

proposed method with respect to the number of subtrees. As the number of subtrees increases, the error E_{feat} calculated using Eq. (5) decreases because the appropriate subtree for a given dataset is selected, and the registration process optimizes the parameters with the selected subtree.

Chapter 6. Conclusion

In this paper, we presented a 2D–3D registration algorithm between pre-operative 3D CTA scans and intra-operative 2D DSA images for liver catheterization. The proposed approach improves the accuracy of the registration by detecting the areas of interest in the 3D vascular structure used for the registration process. The structure constructed from the 3D CTA scans is divided into several subtrees with respect to their connectivity. In the registration process, the dissimilarity of each subtree with a given 2D DSA is computed on the basis of the distance difference between the centerlines from the DSA and a projection of the 3D subtree. Then, the subtree with the smallest dissimilarity is selected as the best matched subtree. Subsequently, a fine registration between the selected subtree and the 2D centerlines is conducted.

The overall vascular structure is very complex, which induces a large number of overlaps and false crossings in the projection onto a 2D detector plane. Thus, it is difficult to match the 3D vascular structure with the projected vessels. Moreover, a DSA displays only

a part of the vascular structure where a catheter currently moves. Therefore, the ranges to be displayed in the CTA and DSA images are very different. The cost function should be designed with this condition. However, the complex structure of vessels leads to a false local minima in the optimization. From this viewpoint, the proposed algorithm has novel features. By separating a structure into several parts, the range of a 3D subtree becomes similar to that of a DSA image. The projection of one subtree preserves its shape without any overlaps between other subtrees and reduces false junctions. Therefore, the proposed method finds the correct subtree to be matched with a given DSA image. Subsequently, the fine registration is conducted with only the relevant vessels with the DSA image, and thus, the registration accuracy is improved considerably.

The experimental results of this study demonstrate that the proposed algorithm can accurately identify an appropriate subtree and find the correct transformation parameters. The proposed method shows good accuracy and convergence with a simple cost function because it focuses only on the interested part of vessels.

Bibliography

[1] H. L. Abrams, Abrams' angiography: interventional radiology, S. Baum and M. J. Pentecost, Eds., Lippincott Williams & Wilkins, 2006.

[2] K. A. Smith and H. S. Kim, "Interventional radiology and image-guided medicine: interventional oncology," *In Seminars in Oncology,* vol. 38, no. 1, pp. 151-162, February 2011.

[3] L. Marelli, R. Stigliano, C. Triantos, M. Senzolo, E. Cholongitas, N. Davies, J. Tibballs, T. Meyer, D. W. Patch and A. K. Burroughs, "Transarterial therapy for hepatocellular carcinoma: which technique is more effective? A systematic review of cohort and randomized studies," *Cardiovascular and interventional radiology,* vol. 30, no. 1, pp. 6-25, 2007.

[4] E. K. Abdalla, M. E. Hicks and J. N. Vauthey, "Portal vein embolization: rationale, technique and future prospects," *British journal of surgery,* vol. 88, no. 2, pp. 165-175, 2001.

[5] R. Avritscher, T. de Baere, R. Murthy, F. Deschamps and D. C. Madoff, "Percutaneous transhepatic portal vein embolization: rationale, technique, and outcomes," *Seminars in interventional radiology,* vol. 25, no. 2, pp.

132-145, June 2008.

[6] P. C. Lebby, Brain imaging: a guide for clinicians, Oxford University Press, 2013.

[7] D. Green and D. Parker, "CTA and MRA: visualization without catheterization," *In Seminars in Ultrasound, CT and MRI,* vol. 24, no. 4, pp. 185-191, 2003.

[8] A. M. Covey, L. A. Brody, G. I. Getrajdman, C. T. Sofocleous and K. T. Brown, "Incidence, patterns, and clinical relevance of variant portal vein anatomy," *American Journal of Roentgenology,* vol. 183, no. 4, pp. 1055-1064, October 2004.

[9] D. Sahani, A. Mehta, M. Blake, S. Prasad, G. Harris and S. Saini, "Preoperative Hepatic Vascular Evaluation with CT and MR Angiography: Implications for Surgery 1," *Radiographics,* vol. 24, no. 5, pp. 1367-1380, September 2004.

[10] D. C. Madoff, E. K. Abdalla, M. J. Wallace, C. S. Ng, D. Ribero and J.-N. Vauthey, "Portal vein embolization: a preoperative approach to improve the safety of major hepatic resection," *Current Medical Imaging Reviews,* vol. 2, no. 4, pp. 385-404, November 2006.

[11] N. Abi-Jaoudeh, J. Kruecker, S. Kadoury, H. Kobeiter, A. M. Venkatesan, E. Levy and B. J. Wood, "Multimodality image fusion-guided procedures: technique, accuracy, and

applications," *Cardiovascular and interventional radiology,* vol. 35, no. 5, pp. 986–998, 2012.

[12] V. Tacher, M. Lin, N. Bhagat, N. A. Jaoudeh, A. Radaelli, N. Noordhoek, B. Carelsen, B. J. Wood and J.–F. Geschwind, "Dual–phase cone–beam computed tomography to see, reach, and treat hepatocellular carcinoma during drug–eluting beads transarterial chemo–embolization," *JoVE (Journal of Visualized Experiments),* vol. 82, pp. e50795–e50795, 2013.

[13] J. A. Maintz and M. A. Viergever, "A survey of medical image registration," *Medical Image Analysis ,* vol. 2, no. 1, pp. 1–36, 1998.

[14] P. Markelj, D. Tomaževič, B. Likar and F. Pernuš, "A review of 3D/2D registration methods for image–guided interventions," *Medical image analysis,* vol. 16, no. 3, pp. 642–661, April 2012.

[15] S. Matl, R. Brosig, M. Baust, N. Navab and S. Demirci, "Vascular image registration techniques: A living review," *Medical Image Analysis,* vol. 35, pp. 1–17, 2017.

[16] J. M. Fitzpatrick, D. L. Hill and C. R. Maurer Jr, "Image registration," *Handbook of medical imaging,* vol. 2, pp. 447–513, 2000.

[17] D. A. Forsyth and J. Ponce, Computer vision: a modern

approach, Prentice Hall Professional Technical Reference, 2002.

[18] J. V. Byrne, C. Colominas, J. Hipwell, T. Cox, J. A. Noble, G. P. Penney and D. J. Hawkes, "Assessment of a technique for 2D-3D registration of cerebral," *The British journal of radiology ,* vol. 77, pp. 123-128, 2014.

[19] A. A. Goshtasby, 2-D and 3-D image registration: for medical, remote sensing, and industrial applications, John Wiley & Sons, 2005.

[20] M. Goitein, M. Abrams, D. Rowell, H. Pollari and J. Wiles, "Multi-dimensional treatment planning: II. Beam's eye-view, back projection, and projection through CT sections," *International Journal of Radiation Oncology* Biology* Physics,* vol. 9, no. 6, pp. 789-797, 198..

[21] Y. Kita, D. L. Wilson and J. A. Noble, "Real-time Registration of 3D Cerebral Vessels to X-ray Angiograms," in *International Conference on Medical Image Computing and Computer-Assisted Intervention*, 1998.

[22] A. Liu, E. Bullitt and S. M. Pizer, "3D/2D Registration Via Skeletal Near Projective Invariance in Tubular Objects," in *International Conference on Medical Image Computing and Computer-Assisted Intervention*, 1998.

[23] R. A. McLaughlin, J. Hipwell, G. P. Penney, K. Rhode, A. Chung, J. A. Noble and D. J. Hawkes, "Intensity-based

Registration versus Feature-based Registration for Neurointerventions," in *Med. Image. Understanding Analysis*, 2001.

[24] R. A. McLaughlin, J. Hipwell, D. J. Hawkes, J. A. Noble, J. V. Byrne and T. Cox, "A Comparison of 2D-3D Intensity-Based Registration and Feature-Based Registration for Neurointerventions," in *International Conference on Medical Image Computing and Computer-Assisted Intervention*, 2002.

[25] J. Feldmar, G. Malandain, N. Ayache, S. Fernández-Vidal, E. Maurincomme and Y. Trousset, "Matching 3D MR Angiography Data and 2D X-ray Angiograms," in *CVRMed-MRCAS'97*, 1997.

[26] E. Kerrien, M.-O. Berger, E. Maurincomme, L. Launay, R. Vaillant and L. Picard, "Fully Automatic 3D/2D Subtracted Angiography Registration," in *International Conference on Medical Image Computing and Computer-Assisted Intervention*, 1999.

[27] C. M. Hentschke and K. D. Tönnies, "Automatic 2D-3D Registration of Cerebral DSA Data Sets," in *Bildverarbeitung für die Medizin*, 2010.

[28] J. H. Hipwell, G. P. Penney, R. A. McLaughlin, K. Rhode, P. Summers, T. C. Cox, J. V. Byrne, J. A. Noble and D. J.

Hawkes, "Intensity-Based 2-D-3-D Registration of Cerebral Angiograms," *IEEE transactions on medical imaging,* vol. 22, no. 11, pp. 1417-1426, 2003.

[29] L. Lemieux, R. Jagoe, D. R. Fish, N. D. Kitchen and D. G. T. Thomas, "A patient-to-computed-tomography image registration method based on digitally reconstructed radiographs," *Medical physics,* vol. 21, no. 11, pp. 1749-1760, 1994.

[30] L. M. G. Brown and T. E. Boult, "Registration of Planar Film Radiographs with Compted Tomography," in *Mathematical Methods in Biomedical Image Analysis*, 1996.

[31] T. M. Buzug, J. Weese, C. Fassnacht and C. Lorenz, "Image Registration: Convex Weighting Functions for Histogram-Based Similarity Measures," in *CVRMed-MRCAS'97*, 1997.

[32] W. M. Wells, P. Viola, H. Atsumi, S. Nakajima and R. Kikinis, "Multi-modal volume registration by maximization of mutual information," *Medical image analysis,* vol. 1, no. 1, pp. 35-51, 1996.

[33] J. Weese, G. P. Penney, P. Desmedt, T. M. Buzug, D. L. G. Hill and D. J. Hawkes, "Voxel-Based 2-D/3-D Registration of Fluoroscopy Images and CT Scans for Image-Guided Surgery," *IEEE transactions on information technology in biomedicine ,* vol. 1, no. 4, pp. 284-293,

1997.

[34] G. P. Penney, J. Weese, J. A. Little, P. Desmedt and D. L. G. Hill, "A Comparison of Similarity Measures for Use in 2-D-3-D Medical Image Registration," *IEEE transactions on medical imaging,* vol. 17, no. 4, pp. 586-595, 1998.

[35] U. Mitrović, F. Pernuš, B. Likar and Ž. Špiclin, "Simultaneous 3D-2D image registration and C-arm calibration: Application to endovascular image-guided interventions," *Medical physics,* vol. 42, no. 11, pp. 6433-6447, 2015.

[36] R. A. McLaughlin, J. Hipwell, D. J. Hawkes, J. A. Noble, J. V. Byrne and T. C. Cox, "A comparison of a similarity-based and a feature-based 2-D-3-D registration method for neurointerventional use," *Medical Imaging, IEEE Transactions on,* vol. 24, no. 8, pp. 1058-1066, August 2005.

[37] H. M. Chan, A. C. S. Chung, S. C. H. Yu and W. M. Wells III, "2D-3D vascular registration between digital subtraction angiographic (DSA) and magnetic resonance angiographic (MRA) images," in *Biomedical Imaging: Nano to Macro, 2004. IEEE International Symposium* , 2004.

[38] K. K. Lau and A. C. S. Chung, "A global optimization strategy for 3D-2D registration of vascular images," in *BMVC*, 2006.

[39] C. Florin, J. Williams, A. Khamene and N. Paragios, "Registration of 3D Angiographic and X-Ray Images Using Sequential Monte Carlo Sampling," in *International Workshop on Computer Vision for Biomedical Image Applications*, 2005.

[40] H. Sundar, A. Kharmene, C. Xu, F. Sauer and C. Davatzikos, "A novel 2D-3D registration algorithm for aligning fluoro images with 3D pre-op CT/MR images," in *Meidical Imaging*, 2006.

[41] U. Mitrovic, Z. Spiclin, B. Likar and F. Pernus, "3D-2D registration of cerebral angiograms: a method and evaluation on clinical images," *Medical Imaging, IEEE Transactions on,* vol. 32, no. 8, pp. 1550-1563, August 2013.

[42] U. Mitrović, Ž. Špiclin, B. Likar and F. Pernuš, "Method for 3D-2D Registration of Vascular Images: Application to 3D Contrast Agent Flow Visualization," in *Workshop on Clinical Image-Based Procedures*, 2012.

[43] M. Groher, N. Padoy, T. F. Jakobs and N. Navab, "New CTA protocol and 2D-3D registration method for liver catheterization," in *Medical Image Computing and Computer-Assisted Intervention*, 2006.

[44] J. Jomier, E. Bullitt, M. V. Horn, C. Pathak and S. R. Aylward, "3D/2D model-to-image registration applied to

TIPS surgery," in *Medical Image Computing and Computer-Assisted Intervention*, 2006.

[45] M. Groher, F. Bender, R.-T. Hoffmann and N. Navab, "Segmentation-Driven 2D-3D Registration for Abdominal Catheter Interventions," in *International Conference on Medical Image Computing and Computer-Assisted Intervention*, 2007.

[46] M. Groher, D. Zikic and N. Navab, "Deformable 2D-3D registration of vascular structures in a one view scenario," *Medical Imaging, IEEE Transactions on,* vol. 28, no. 6, pp. 847-860, June 2009.

[47] M. Groher, M. Baust, D. Zikic and N. Navab, "Monocular Deformable Model-to-Image Registration of Vascular Structures," in *International Workshop on Biomedical Image Registration*, 2010.

[48] P. Ambrosini, D. Ruijters, W. J. Niessen, A. Moelker and T. van Walsum, "Continuous roadmapping in liver TACE procedures using 2D-3D catheter-based registration," *International journal of computer assisted radiology and surgery,* vol. 10, no. 9, pp. 1357-1370, September 2015.

[49] B. Desjardins and E. A. Kazerooni, "ECG-Gated Cardiac CT," *American Journal of Roentgenology,* vol. 182, no. 4, pp. 993-1010, 2004.

[50] L. Duong, R. Liao, H. Sundar, B. Tailhades, A. Meyer and

C. Xu, "Curve-based 2D-3D Registration of Coronary Vessels for Image Guided Procedure," in *SPIE Medical Imaging*, 2009.

[51] G.-A. Turgeon, G. Lehmann, G. Guiraudon, M. Drangova, D. Holdsworth and T. Peters, "2D-3D registration of coronary angiograms for cardiac procedure planning and guidance," *Medical Physics,* vol. 32, no. 12, pp. 3737-3749, December 2005.

[52] C. T. Metz, M. Schaap, S. Klein, A. C. Weustink, N. R. Mollet, C. Schultz, R. J. van Geuns, P. W. Serruys, T. van Walsum and W. J. Niessen, "GPU accelerated alignment of 3-D CTA with 2-D X-ray data for improved guidance in coronary interventions," in *IEEE International Symposium on Biomedical Imaging: From Nano to Macro*, 2009.

[53] D. Ruijters, B. M. ter Haar Romneny and P. Suetens, "Vesselness-based 2D-3D registration of the coronary arteries," *International journal of computer assisted radiology and surgery,* vol. 4, no. 4, pp. 391-397, June 2009.

[54] T. Aksoy, G. Unal, S. Demirci, N. Navab and M. Degetekin, "Template-based CTA to x-ray angio rigid registration of coronary arteries in frequency domain with automatic x-ray segmentation," *Medical physics,* vol. 40, no. 10, p. 101903, 2013.

[55] G. Dibildox, N. Baka, M. Punt, J.-P. Aben, C. Schultz, W. Niessen and T. van Walsum, "3D/3D registration of coronary CTA and biplane XA reconstructions for improved image guidance," *Medical physics,* vol. 41, no. 9, p. 091909, 2014.

[56] Y. Khoo and A. Kapoor, "Non-iterative rigid 2D/3D point-set registration using semidefinite programming," *IEEE Transactions on Image Processing,* vol. 25, no. 7, pp. 2956-2970, 2016.

[57] A. F. Frangi, W. J. Nessen, K. L. Vincken and M. A. Viergever, "Multiscale vessel enhancement filtering," in *Medical Image Computing and Computer-Assisted Interventation*, 1998.

[58] C. T. Metz, M. Schaap, S. Klein, L. A. Neefjes, E. Capuano, C. Schultz, R. J. van Geuns, P. W. Serruys, T. van Walsum and W. J. Niessen, "Patient specific 4D coronary models from ECG-gated CTA data for intra-operative dynamic alignment of CTA with X-ray images," in *International Conference on Medical Image Computing and Computer-Assisted Intervention*, 2009.

[59] C. Metz, M. Schaap, S. Klein, P. Rijnbeek, L. Neefjes, N. Mollet, C. Schultz, P. Serruys, W. Niessen and T. van Walsum, "Alignment of 4D coronary CTA with monoplane X-ray angiography," in *Workshop on Augmented*

Environments for Computer-Assisted Interventions, 2011.

[60] R. Toledo, P. Radeva, C. Von Land and J. Vilanueva, "3D dynamic model of the coronary tree," in *Computers in Cardiology*, 1998.

[61] D. Rivest-Henault, H. Sundar and M. Cheriet, "Nonrigid 2D/3D registration of coronary artery models with live fluoroscopy for guidance of cardiac interventions," *Medical Imaging, IEEE Transactions on,* vol. 31, no. 8, pp. 1557-1572, August 2012.

[62] J. Hadida, C. Desrosiers and L. Duong, "Stochastic 3D motion compensation of coronary arteries from monoplane angiograms," in *International Conference on Medical Image Computing and Computer-Assisted Intervention*, 2012.

[63] H.-R. Kim, M.-S. Kang and M.-H. Kim, "Non-rigid registration of vascular structures for aligning 2D X-ray angiography with 3D CT angiography," in *International Symposium on Visual Computing*, 2014.

[64] P. M. Djuric, J. H. Kotecha, J. Zhang, Y. Huang, T. Ghirmai, M. F. Bugallo and J. Miguez, "Particle filtering," *IEEE signal processing magazine,* vol. 20, no. 5, pp. 19-38, 2003.

[65] R. van Uitert and I. Bitter, "Subvoxel precise skeletons of volumetric data based on fast marching methods," *Medical physics,* vol. 34, no. 2, pp. 627-638, February 2007.

[66] D. Lesage, E. D. Angelini, I. Bloch and G. Funka-Lea, "A review of 3D vessel lumen segmentation techniques: Models, features and extraction schemes," *Medical image analysis,* vol. 13, no. 6, pp. 819-845, 2009.

[67] T. McInerney and D. Terzopoulos, "Deformable models in medical image analysis: a survey," *Medical image analysis,* vol. 1, no. 2, pp. 91-108, 1996.

[68] S. D. Olabarriaga, M. Breeuwer and W. J. Niessen, "Minimum cost path algorithm for coronary artery central axis tracking in CT images," in *International Conference on Medical Image Computing and Computer-Assisted Intervention*, 2003.

[69] O. Wink, W. J. Niessen and M. A. Viergever, "Multiscale vessel tracking," *IEEE Transactions on Medical Imaging,* vol. 23, no. 1, pp. 130-133, 2004.

[70] O. Wink, W. J. Niessen, B. Verdonck and M. A. Viergever, "Vessel axis determination using wave front propagation analysis," in *International Conference on Medical Image Computing and Computer-Assisted Intervention*, 2001.

[71] Y. Sato, S. Nakajima, N. Shiraga, H. Atsumi, S. Yoshida, T. Koller, G. Gerig and R. Kikinis, "Three-dimensional multi-scale line filter for segmentation and visualization of curvilinear structures in medical images," *Medical image analysis,* vol. 2, no. 2, pp. 143-168, 1998.

[72] C. Lorenz, I.-C. Carlsen, T. M. Buzug, C. Fassnacht and J. Weese, "A multi-scale line filter with automatic scale selection based on the Hessian matrix for medical image segmentation," in *International Conference on Scale-Space Theories in Computer Vision*, 1997.

[73] H. Blum, "A transformation for extracting descriptors of shape," in *Models for the Perception of Speech and Visual Forms*, 1967.

[74] T. Y. Kong and A. Rosenfeld, "Digital topology: Introduction and survey," *Computer Vision, Graphics, and Image Processing,* vol. 48, no. 3, pp. 357-393, 1989.

[75] E. R. Davies and A. N. Plummer, "Thinning algorithms: a critique and a new methodology," *Pattern Recognition,* vol. 14, no. 1, pp. 53-63, 1981.

[76] T.-C. Lee, R. L. Kashyap and C.-N. Chu, "Building skeleton models via 3-D medial surface axis thinning algorithms," *CVGIP: Graphical Models and Image Processing,* vol. 56, no. 6, pp. 462-478, 1994.

[77] D. Selle, B. Preim, A. Schenk and H.-o. Peitgen, "Analysis of vasculature for liver surgical planning," *Medical Imaging, IEEE Transactions on,* vol. 21, no. 11, pp. 1344-1357, November 2002.

[78] M. A. Gülsün and H. Tek, "Robust vessel tree modeling," in

Medical Image Computing and Computer-Assisted Intervention, 2008.

[79] D. Adalsteinsson, A fast level set method for propagating interfaces, CA: University of California Berkeley, 1994.

[80] T. Aach, D. Kunz, R. Florent and S. Makram-Ebeid, "Noise Reduction and Image Enhancement Algorithms for Low-Dose X-Ray Fluoroscopy," *Bildverarbeitung für die Medizin,* pp. 95-100, 1996.

[81] V. Bhaskaran and K. Konstantinides, Image and video compression standards: algorithms and architectures. Vol. 408, Springer Science & Business Media, 1997.

[82] D. Marsh, Applied geometry for computer graphics and CAD, Springer Science & Business Media, 2006.

[83] R. L. Siddon, "Fast calculation of the exact radiological path for a three-dimensional CT array," *Medical physics,* vol. 12, no. 2, pp. 252-255, March 1985.

[84] A. Fitzgibbon, "Robust registration of 2D and 3D point sets," *Image and Vision Computing,* vol. 21, no. 13, pp. 1145-1153, December 2003.

[85] P. Felzenszwalb and D. Huttenlocher, Distance transforms of sampled functions, Cornell University, 2004.

[86] F. J. Gravetter and L. B. Wallnau, Statistics for the

behavioral sciences, Cengage Learning, 2016.

[87] W. H. Kruskal and W. A. Wallis, "Use of ranks in one-criterion variance analysis," *Journal of the American statistical Association,* vol. 47, no. 260, pp. 583-621, 1952.

초 록

혈관 조영술은 X-ray 등의 영상 기술의 도움을 받아 최소한의 침습만으로 질병을 진단 및 치료함으로써 환자의 신체적 부담감을 줄이고 효율적인 치료를 가능하게 하는 진단 및 치료 방식이다. 시술을 위해서는 카데터를 신체 내의 치료가 필요한 위치까지 이동시켜야 하는데 카데터의 경로를 판단할 수 있도록 혈관이 조영된 2D X-ray 영상이 주로 사용된다. 이 때 혈관의 전체적인 구조나 연결 관계는 2D 영상만으로는 판단이 어렵기 때문에 시술 전 촬영된 3D 혈관 조영 영상을 현재의 2D 영상 위로 투영시키는 로드맵 기술이 사용될 수 있다. 정확한 로드맵 생성을 위해서는 현재 투영되고 있는 2D 영상과 시술 전 획득한 3D 영상 간의 정합 알고리즘이 필수적으로 요구된다. 그러나 복잡한 3D 혈관을 2D로 투영시키는 과정에서 혈관의 연결관계 파악이 힘들어지고 이는 정확한 정합 결과를 구하기 어렵게 만든다. 본 논문에서는 이러한 문제점을 해결하기 위하여 전체 3D 혈관 구조로부터 현재의 2D 영상에 매칭되는 일부의 혈관 영역 만을 선택하고 선택된 영역만을 기준으로 정합을 수행하게 된다. 이는 2D 영상과 연관된 영역만을 정합에 이용함으로써 정합의 정확도를 크게 향상시킬 수 있게 된다. 2D 영상에 적절한 3D 혈관 영역을 찾기 위해서, 우선 3D 영상으로부터 혈관을 분할하고 이로부터 혈관의 센터라인을 추출해낸다. 이를 트리 모델로 구성한 뒤 혈관의 연결관계를 고려하여 여러 개의

서브트리로 나누게 된다. 그리고 시술 중에 획득한 2D 영상과 가장 적합한 서브트리를 찾기 위하여, 2D 영상으로부터 추출한 2D 혈관의 센터라인과 서브트리 각각과의 정합 과정을 수행하게 된다. 각 서브트리에대한 정합 수행 후 가장 유사도가 높은 서브트리가 2D 혈관과 매칭되는 3D 혈관 영역이라 판단한다. 마지막으로, 선택된 서브트리에 대하여 서브트리와 2D 혈관 센터라인 간의 정밀 정합을 수행하게 된다. 일부 영역만으로 계산된 정합 파라미터는 전체 혈관 구조에 대해서도 정확한 정합 결과를 보여준다. 또한, 2D 혈관과 대응되는 일부 영역만으로 정합을 수행함으로써 정합 과정의 수렴 속도는 빨라지고 정확도는 높아지게 된다. 총 10개의 환자 데이터에 대해 제안된 알고리즘을 검증한 결과 평균 정합 오차 2.34 ± 1.94 mm를 얻을 수 있었다. 제안된 정합 알고리즘은 기존에 제안된 2D-3D 정합 알고리즘과 비교하여 매우 높은 정합 정확도를 보이는 것을 확인할 수 있다.

주요어 : 2D-3D 정합, 혈관 구조, 혈관 분할, 혈관조영술
학 번 : 2013-30228